

# Wake transitions behind a cube at low and moderate Reynolds numbers

Qingrui Meng<sup>1</sup>, Hongwei An<sup>1</sup>, Liang Cheng<sup>1,2,†</sup> and Mehrdad Kimiaei<sup>3</sup>

<sup>1</sup>School of Engineering, University of Western Australia, 35 Stirling Highway, Crawley, WA 6009, Australia

<sup>2</sup>DUT–UWA Joint Research Centre, State Key Laboratory of Coastal and Offshore Engineering, Dalian University of Technology, No. 2 Linggong Road, 116024 Dalian, PR China

<sup>3</sup>Oceans Graduate School, University of Western Australia, 35 Stirling Highway, Crawley, WA 6009, Australia

(Received 14 October 2020; revised 15 March 2021; accepted 4 May 2021)

Wake transitions behind an isolated cube are investigated numerically over a range of Reynolds number ( $Re$ ) 1–400. Four flow regimes, namely the orthogonal symmetry–steady ( $1 \leq Re \leq 205$ ), planar symmetry–steady (PSS,  $210 \leq Re \leq 250$ ), hairpin-vortex shedding (HS,  $255 \leq Re \leq 305$ ) and chaotic vortex shedding ( $Re \geq 310$ ) regimes, are identified according to spatial symmetries and temporal development of the flow. A weakly nonlinear stability analysis, through a coupled pitchfork bifurcation model proposed in the present study, reveals that the bifurcation to the PSS regime is supercritical and the planar symmetry is retained in the PSS regime because stable points (four) exist only on the two symmetry planes perpendicular to the side faces of the cube. The supercritical Hopf bifurcation to the HS regime is induced by the excessive accumulation of circulation in the downstream tips of merged streamwise vortex tubes behind the cube that subsequently attract the vortex tubes of opposite signs to cut the tips off from them, leading to alternate shedding of streamwise vortex tubes. The planar symmetry observed in the PSS regime is preserved in the three vortex shedding states identified in the HS regime, i.e. single-frequency shedding ( $255 \leq Re \leq 280$ ), quasi-periodic shedding ( $282 \leq Re \leq 285$ ) and the high-order synchronised shedding (HS2,  $289 \leq Re \leq 305$ ). A cascade of period doubling and period halving is discovered in the HS2 state, prior to the flow bifurcation to the chaotic vortex shedding regime, where the planar symmetry is broken. The critical  $Re$  values for the bifurcations to PSS and HS regimes are estimated to be  $Re \approx 207.0$  and  $252.0$ , respectively, through linear interpolation of the growth rate of flow instabilities.

**Key words:** bifurcation, vortex shedding, flow–structure interactions

† Email address for correspondence: [liang.cheng@uwa.edu.au](mailto:liang.cheng@uwa.edu.au)

### 1. Introduction

Compared with the flow past a sphere, steady approaching flow around a cube has not been studied extensively, possibly because flow around a cube is less commonly encountered than its counterpart past a sphere in practical applications. This perspective, however, does not necessarily represent a fair reflection of the significance of flow around the cube. The sharp edges and discontinuous symmetry (i.e. finite reflection planes) of the cube lead to a different class of wake characteristics that are common for cuboids but not for smooth surface objects such as a sphere. Flows around cuboids are common in engineering applications in fact, for example, low speed positioning underwater vehicles, buoyancy blocks and free falling of non-spherical particles. The underwater vehicle and buoyancy block can be controlled and constrained by some means to keep steady in constant currents, and the free-falling and free-rising patterns of non-spherical particles can also be in a vertical path depending on the solid-to-fluid density ratio and Galileo number (Seyed-Ahmadi & Wachs 2019), all of which implies they can be represented by the ideal scenario of steady flow past a stationary cuboid. Therefore, a sound understanding of flow around the cube is important both fundamentally and practically.

An isolated and stationary cube placed in the uniform flow is illustrated in figure 1. A simple dimensional analysis shows that the flow regime is only governed by Reynolds number  $Re$ , which is defined as  $UL/\nu$  with  $U$  denoting the velocity of the undisturbed incoming flow,  $L$  the edge length of the cube and  $\nu$  the kinematic viscosity of the fluid (the diameter of a sphere of the same volume is also used as the reference length to study freely moving cubes, e.g. Seyed-Ahmadi & Wachs 2019). The existing studies (e.g. Saha 2004; Klotz *et al.* 2014; Seyed-Ahmadi & Wachs 2019; Khan, Sharma & Agrawal 2020) have demonstrated that the flow is steady at low  $Re$  and becomes unsteady when  $Re$  exceeds a critical value. The flow features in both steady and unsteady states are dictated by the geometric symmetries of the cube. A Cartesian coordinate system  $(x, y, z)$  is established at the centre of the cube in figure 1 to describe the geometric symmetries. Two types of symmetries exist in the planes perpendicular to the  $x$ -axis. One is the rotational symmetry with respect to the  $x$ -axis that forms a cyclic group of  $\pi/2$  and the other is the reflection symmetry with respect to any of the planes  $y = 0, z = 0, y = z$  and  $y = -z$ . The combination of the rotational and reflection symmetries brews out a dihedral group  $D_4$  (for the dihedral group, see Armstrong 2013), which is a finite subgroup of the special orthogonal group in two dimensions, i.e.  $SO(2)$ . Hereinafter, we employ ‘orthogonal symmetry’ to refer to the symmetry in  $D_4$ . By defining the velocity and pressure fields as  $(u_x, u_y, u_z, p)$  and spatio-temporal coordinates as  $(x, y, z, t)$ , we denote the rotational symmetry conditions of the flow as  $\mathcal{G}^r$  in (1.1)–(1.4) with respect to the rotational angle  $\vartheta$  around the  $x$ -axis in a counter-clockwise direction and the reflection symmetry conditions as  $\mathcal{G}^s$  in (1.5)–(1.8), with the subscripts denoting the corresponding symmetric planes, i.e.

$$\mathcal{G}_{\vartheta=0}^r : (u_x, u_y, u_z, p)(x, y, z, t) = (u_x, u_y, u_z, p)(x, y, z, t), \tag{1.1}$$

$$\mathcal{G}_{\vartheta=\pi/2}^r : (u_x, u_y, u_z, p)(x, y, z, t) = (u_x, -u_z, u_y, p)(x, -z, y, t), \tag{1.2}$$

$$\mathcal{G}_{\vartheta=\pi}^r : (u_x, u_y, u_z, p)(x, y, z, t) = (u_x, -u_y, -u_z, p)(x, -y, -z, t), \tag{1.3}$$

$$\mathcal{G}_{\vartheta=3\pi/2}^r : (u_x, u_y, u_z, p)(x, y, z, t) = (u_x, u_z, -u_y, p)(x, z, -y, t), \tag{1.4}$$

$$\mathcal{G}_{y=0}^s : (u_x, u_y, u_z, p)(x, y, z, t) = (u_x, -u_y, u_z, p)(x, -y, z, t), \tag{1.5}$$

$$\mathcal{G}_{z=0}^s : (u_x, u_y, u_z, p)(x, y, z, t) = (u_x, u_y, -u_z, p)(x, y, -z, t), \tag{1.6}$$

$$\mathcal{G}_{y=z}^s : (u_x, u_y, u_z, p)(x, y, z, t) = (u_x, u_z, u_y, p)(x, z, y, t), \tag{1.7}$$

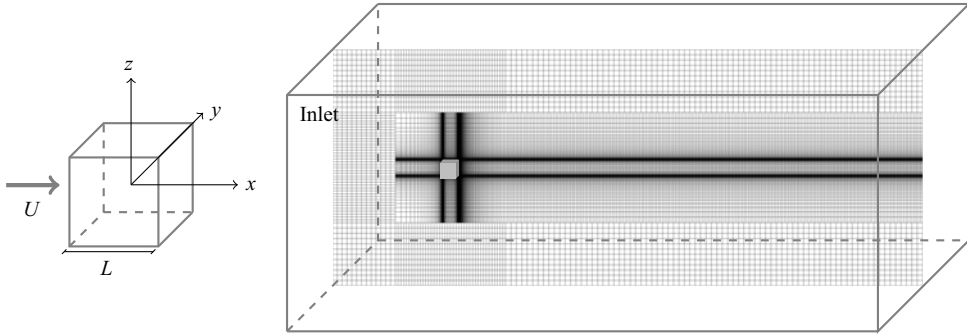


Figure 1. Schematics of flow past the cube, compute domain and the compound mesh on the middle slice.

$$\mathcal{G}_{y=-z}^s : (u_x, u_y, u_z, p)(x, y, z, t) = (u_x, -u_z, -u_y, p)(x, -z, -y, t). \quad (1.8)$$

Considerable understanding about the flow at low  $Re$  has been achieved based on the aforementioned studies (Saha 2004; Klotz *et al.* 2014; Seyed-Ahmadi & Wachs 2019; Khan *et al.* 2020). Table 1 provides a brief summary of flow regimes identified previously. There appears a lack of consistency in naming the flow regimes among these studies. To facilitate further discussions, we unify the names of those regimes in table 1 based on the spatial symmetries and temporal development of the flow. The existing studies showed that the flow undergoes two major bifurcations in the sequence of increasing  $Re$ . The first one is a regular bifurcation featured by a transition from orthogonal symmetry–steady (OSS) flow to planar symmetry–steady (PSS) flow, where the orthogonal symmetry is broken and one reflection symmetry is retained in the PSS flow. The second one is a Hopf bifurcation, where the flow becomes unsteady with shedding of hairpin-shaped vortices into the wake from the cube surface. This regime is thereby defined as hairpin-vortex shedding (HS) flow. Klotz *et al.* (2014) investigated the nature of these two bifurcations through the dependence of the squared amplitude of the global perturbation on Reynolds number and found both bifurcations were supercritical. As demonstrated by Saha (2004) and Klotz *et al.* (2014), the flow in the HS regime retains one of the reflection symmetries. As  $Re$  is further increased in the HS regime, the reflection symmetry is broken and the vortex shedding from the cube becomes chaotic, leading to a transition to the chaotic shedding (CS) regime (Khan *et al.* 2020).

In addition to the observations about the flow features in every regime, Klotz *et al.* (2014) conducted a series of analyses based on their experimental data. The flow transitions were characterised by two different methods. One was the linear dependence of longitudinal enstrophy on the Reynolds number, and the other was the energy correlation of the azimuthal Fourier modes of streamwise vorticity. It is interesting to note Landau’s amplitude equation (Stuart 1960; Watson 1960) is effective in a relatively wider interval of Reynolds numbers, which can facilitate the determination of critical Reynolds numbers for the supercritical bifurcations.

Despite the good understanding of the flow achieved so far, a number of important issues related to the flow have not yet been resolved. For example, there is a lack of understanding on the flow mechanisms behind the vortex shedding. In addition, it is not clear how the flow bifurcations occur towards the chaotic regime. The above aspects motivate the present study. Specifically, direct numerical simulations (DNS) are conducted over  $Re$  1–400 to investigate those issues. Despite the obvious relevance of high-Reynolds-number flows to engineering applications, a sound understanding of flow mechanisms behind vortex

	Regime I	Regime II	Regime III	Regime IV
Saha (2004)	Steady symmetric flow ( $20 \leq Re \leq 216$ )	Steady asymmetric flow ( $218 \leq Re \leq 265$ )	Unsteady flow ( $270 \leq Re \leq 300$ )	—
Richter & Nikrityuk (2012)	Flow having two symmetry planes	Loss of flow symmetry (critical $Re$ for I→II is in 200–250)	Laminar-unsteady flow (critical $Re$ for II→III is in 245–260)	—
Klotz <i>et al.</i> (2014)	Base flow  ( $100 \leq Re \lesssim 186$ )	Two counter-rotating vortices flow ( $186 \lesssim Re < 277$ )	Hairpin-vortex shedding ( $277 \leq Re \leq 400$ )	—
Seyed-Ahmadi & Wachs (2019)	Not specified ( $150 \leq Re \leq 180$ )	Not specified ( $190 \leq Re < 225$ )	Not specified ( $225 \leq Re \leq 300$ )	—
Khan <i>et al.</i> (2020)	Steady axisymmetric flow  ( $20 \leq Re \leq 200$ )	Steady non-axisymmetric flow  ( $215 \leq Re \leq 250$ )	Unsteady flow, axisymmetric in one plane and non-axisymmetric in other plane ( $276 \leq Re \leq 300$ )	Unsteady non-axisymmetric flow in streamwise orthogonal planes ( $339 \leq Re \leq 770$ )
Present study	Orthogonal symmetry–steady (OSS) flow	Planar symmetry–steady (PSS) flow	Hairpin-vortex shedding (HS) flow	Chaotic shedding (CS) flow

Table 1. A summary of flow regimes reported in the literature and those identified in the present study. Note that the major focus of Richter & Nikrityuk (2012) was about the drag and heat transfer coefficients for flow past spheres and various non-spherical particles, that of Seyed-Ahmadi & Wachs (2019) was about free-falling and free-rising cubes, and the rest of the studies were concerned with a stationary cube. The critical value from regime II to III in Klotz *et al.* (2014) is inferred as a value less than  $Re = 277$  based on the observation of the peristaltic motion.

shedding in the laminar flow regime and its bifurcation features is pivotal to future studies on high-Reynolds-number flows. The rest of the paper is organised as following. The numerical method is briefly introduced in § 2. The regime map identified in the present study, and the corresponding characteristics of steady and unsteady flows are elaborated in § 3–5 separately. The weakly nonlinear instability analysis is presented in § 6. The main conclusions are drawn in § 7.

## 2. Numerical method

The steady approaching flow around the cube is governed by the incompressible Navier–Stokes equations, which can be written in the following non-dimensional form:

$$\frac{\partial u_i}{\partial x_i} = 0, \tag{2.1}$$

$$\frac{\partial u_i}{\partial t} + u_j \frac{\partial u_i}{\partial x_j} = -\frac{\partial p}{\partial x_i} + \frac{1}{Re} \frac{\partial^2 u_i}{\partial x_j \partial x_j}. \tag{2.2}$$

Here  $u_i$  and  $x_i$  are the velocity and spatial coordinate tensors with  $(u_1, u_2, u_3) = (u_x, u_y, u_z)$  and  $(x_1, x_2, x_3) = (x, y, z)$ ;  $p$  and  $t$  refer to pressure and time, respectively; Reynolds number  $Re$  is defined as  $UL/\nu$ .

The computational domain is exhibited in [figure 1](#) with dimensions of (37.5, 15, 15) in corresponding  $x$ ,  $y$  and  $z$  directions. The centre of the cube is located 7.5 to the inlet, top, bottom and lateral boundaries, and 30 to the outlet boundary. The distances from the origin to the inlet and outlet are justified by referring Saha (2004) and Khan *et al.* (2020), where the corresponding dimensions are (6, 22) and (7.5, 17.5), respectively. The larger distance of 30 to the outlet is deliberately chosen in order to obtain a better visualisation of the wake structure. The dimensions in the  $y$  and  $z$  directions are determined according to Klotz *et al.* (2014), where the blockage effect was shown to be negligible with a blockage ratio of 0.43 %, which is close enough to the present blockage ratio of 0.44 %.

The governing equations are solved numerically by the finite volume method embedded in OpenFOAM v1712 with the pressure-implicit splitting of operators (PISO) algorithm (Issa 1986). The time derivative term is discretised by a combined scheme in which an equal split of the first-order Euler and second-order Crank–Nicolson schemes is adopted. The convection and diffusion terms are discretised by the fourth-order Gaussian cubic and second-order Gaussian linear corrected schemes, respectively. The numerical accuracy is therefore of first order in time and second order in space.

The no-slip boundary conditions of  $u_i = 0$  and  $\partial p/\partial n = 0$  are imposed on the surface of the cube, where  $\partial/\partial n$  represents the normal derivative. The conditions of  $u_i = \delta_{ij}$  ( $\delta_{ij}$  is the Kronecker delta) and  $\partial p/\partial n = 0$  are specified on the inlet boundary, while  $\partial u_i/\partial n = 0$  and  $p = 0$  are enforced on the outlet boundary. The symmetric boundary conditions are imposed on the top, bottom and lateral boundaries. The initial conditions for every simulation are  $u_i = 0$  and  $p = 0$ , except for those mentioned specifically hereinafter.

A compound mesh, which consists of an internal region with refined hexahedral cells and an external region with coarse hexahedral cells, is introduced in order to reduce the computational costs. As shown in [figure 1](#), the dimensions of the internal region are determined as (33.5, 7, 7) by a mesh dependence study, where the simulation results, based on a structural mesh over the entire domain that has the same mesh density as that in the region of (33.5, 7, 7), showed a negligible difference to those based on the compound mesh. The total cell number of the compound mesh is approximately 30 % lower than that used in the structural mesh over the entire domain, leading to significant savings in computational costs without compromising the accuracy of the results. A further mesh dependence study regarding the refinement in the internal region is discussed in § A.

The numerical stability is achieved by limiting the maximum Courant number  $Co_{max} < 1$  throughout the computational domain. The Courant number  $Co$  is defined as

$$Co = \frac{\Delta t}{2\mathcal{V}} \sum |\varphi_i|, \quad (2.3)$$

where  $\mathcal{V}$  is the cell volume and  $\sum |\varphi_i|$  is the summation of absolute volumetric flux through all faces of the considered cell (<https://www.openfoam.com/documentation/guides/latest/doc/guide-fos-field-CourantNo.html>). A time step  $\Delta t = 0.0025$  is adopted to satisfy this stability requirement.

The drag coefficient  $C_d$ , lift coefficient in the  $y$  direction  $C_{l,y}$ , lift coefficient in the  $z$  direction  $C_{l,z}$  and the magnitude of lift coefficients  $C_l$  on the cube are defined to facilitate further discussions,

$$C_d = \frac{F_d}{1/2\rho U^2 L^2}, \quad (2.4)$$

$$C_{l,y} = \frac{F_{l,y}}{1/2\rho U^2 L^2}, \quad (2.5)$$

$$C_{l,z} = \frac{F_{l,z}}{1/2\rho U^2 L^2}, \quad (2.6)$$

$$C_l = (C_{l,y}^2 + C_{l,z}^2)^{1/2}, \quad (2.7)$$

where  $\rho$  is the fluid density, and  $F_d$ ,  $F_{l,y}$  and  $F_{l,z}$  are the forces exerted on the cube in the corresponding directions. It is noted that  $\rho$ ,  $F_d$ ,  $F_{l,y}$  and  $F_{l,z}$  should take the dimensional forms in order to emphasise the physical meaning of the definition of the hydrodynamic coefficients, even though the non-dimensional operation has been introduced above.

### 3. Flow regimes and states

The flow regimes are mapped out over  $Re$  1–400. The  $Re$  ranges and corresponding features of the four regimes identified in the present study are briefly described in [table 2](#). Distinguished by the status of flow separation on the cube surface, the OSS regime is further divided into non-separation (NS), OSS1 and OSS2 states. No flow separation occurs in NS and flow only separates on the rear face of the cube in OSS1. The flow initially separates near the front leading edges of the cube, reattaches on the lateral surfaces and then separates again on the trailing edges of the rear face in OSS2. We hereby define the downstream and upstream flow separations as the primary and secondary separations, respectively. Based on distinct frequency spectra, the HS regime is split into single-frequency shedding (HS1), quasi-periodic shedding (QP) and high-order synchronised shedding (HS2) states. The flow in HS1 is characterised by regular shedding of hairpin vortices and the normalised frequency of the regular shedding is denoted by the Strouhal number  $St_1$ . A low frequency component  $St_2$ , which is incommensurable with  $St_1$ , appears in the QP state. Here  $St_2$  becomes commensurable with  $St_1$  in HS2. A cascade of period doubling and period halving is also observed in the HS2 state. The  $Re$  values for the flow regimes and states as shown in [table 2](#) are determined through variable increments of Reynolds number, i.e.  $\Delta Re$ , between 1 and 20. The flow features and their corresponding physical mechanisms in those flow regimes are further discussed in the following sections.

## 4. Steady flows

### 4.1. Orthogonal symmetry–steady flow

Flow separations in the OSS regime are illustrated by two-dimensional streamlines on the cube faces in [figure 2](#), where representative cases at  $Re = 1, 3, 135$  and  $200$  are employed. The streamlines are derived using the velocity at the cell centre of the first layer of the mesh. The faces of the cube are referred to by  $F_{x^\pm}$ ,  $F_{y^\pm}$  and  $F_{z^\pm}$  with the subscripts corresponding to the outer normal vectors of the faces. When  $Re$  is smaller than a critical value between 1 and 3, the flow is attached as shown in [figure 2\(a\)](#), where the zero streamline diverges from the stagnation point at the centre of  $F_{x^-}$  and converges at the counterpart of the rear face  $F_{x^+}$  in the NS state. The onset of flow separation is observed in the OSS1 state. Initially, at low Reynolds numbers such as  $Re = 3$  in [figure 2\(b\)](#), the separation only occurs on the rear face, as is demonstrated by the streamlines converging to a square outline. When  $Re$  is further increased in OSS1, the primary flow separation point  $S_1$  extends towards the sharp edges of the rear face, as shown in [figure 2\(c\)](#). For the flows in the OSS2 state, a separation bubble on each of the lateral faces is observed in [figure 2\(d\)](#) at  $Re = 200$ , spanning from the secondary separation point  $S_2$  to the reattachment point



Regime	$Re$	State	Symmetry	Dynamical feature
I	1	NS	Orthogonal symmetry	Steady, non-separation
	3–142	OSS1	Orthogonal symmetry	Steady, four pairs of vortices behind the cube
	143–205	OSS2	Orthogonal symmetry	Steady, four pairs of vortices behind the cube, and four pairs of vortices beside the cube
II	210–250	PSS	Planar symmetry	Steady, two counter-rotating vortices
III	255–280	HS1	Planar symmetry	Single-frequency hairpin-vortex shedding
	282, 285	QP	Planar symmetry	QP
	289–305	HS2	Planar symmetry	High-order synchronised hairpin-vortex shedding, superharmonic spectrum, existence of a cascade of period doubling and period halving
IV	310–400	CS	Asymmetric	Chaotic shedding, weak turbulence

Table 2. Transitional states for flow past the cube with Reynolds number varying from 1 to 400.

$R$ , and the reattachment lines are in a parabolic shape. It is also noted that the primary separation lines coincide with the sharp edges of the rear face, while the secondary separation lines are slightly offset from the sharp edges of the front face. This finding is consistent with the observation of flow around a two-dimensional square cylinder by Jiang & Cheng (2020).

The evolutions of the primary separation, secondary separation and reattachment points against  $Re$  are illustrated by quantifying the separation and reattachment angles within the plane  $z = 0$  in figure 3(a), and the length of the secondary recirculation bubble in figure 3(b). The primary separation, secondary separation and reattachment angles, marked respectively as  $\theta_{S_1}$ ,  $\theta_{S_2}$  and  $\theta_R$  in figure 3(b), are defined as positive in the counter-clockwise direction of the  $x$ -axis, while the length of the secondary recirculation bubble is defined as the distance  $l_2$  between  $S_2$  and  $R$ . As shown in figure 3(a),  $\theta_{S_1}$  increases to the value of  $\pi/4$  rapidly after the onset of primary separation, and remains  $\pi/4$  until  $Re$  reaches to the upper bound of the OSS2 state. The occurrence of the OSS2 state is observed with the appearance of the secondary recirculation bubble at  $Re = 143$ . The corresponding secondary separation angle  $\theta_{S_2}$  is observed increasing against  $Re$ , slowly approaching  $3\pi/4$ , while the reattachment angle  $\theta_R$  decreases tending to  $\pi/4$ . In figure 3(b) the length of the recirculation bubble  $l_2$  increases against  $Re$ , and their correlation is nonlinear for  $Re < 155$  while linear for  $Re > 155$ . Although the above evolution trends for the primary and secondary flow separations are demonstrated through the points  $S_1$ ,  $S_2$  and  $R$  on the symmetry plane  $z = 0$ , the trends based on other planes close and parallel to either  $y = 0$  or  $z = 0$  are expected to be similar. The length of the secondary recirculation bubble on other planes will be smaller than that on  $z = 0$ , as implied by the streamlines in figure 2(d).

The spatial structure of the recirculation zones in the OSS regime are illustrated by three-dimensional steady streamlines coloured by the streamwise velocity  $u_x$  in figure 4. The OSS1 state, which only possesses the primary recirculation zone, is presented for  $Re = 135$  in figures 4(a) and 4(b), where four pairs of counter-rotating vortices are

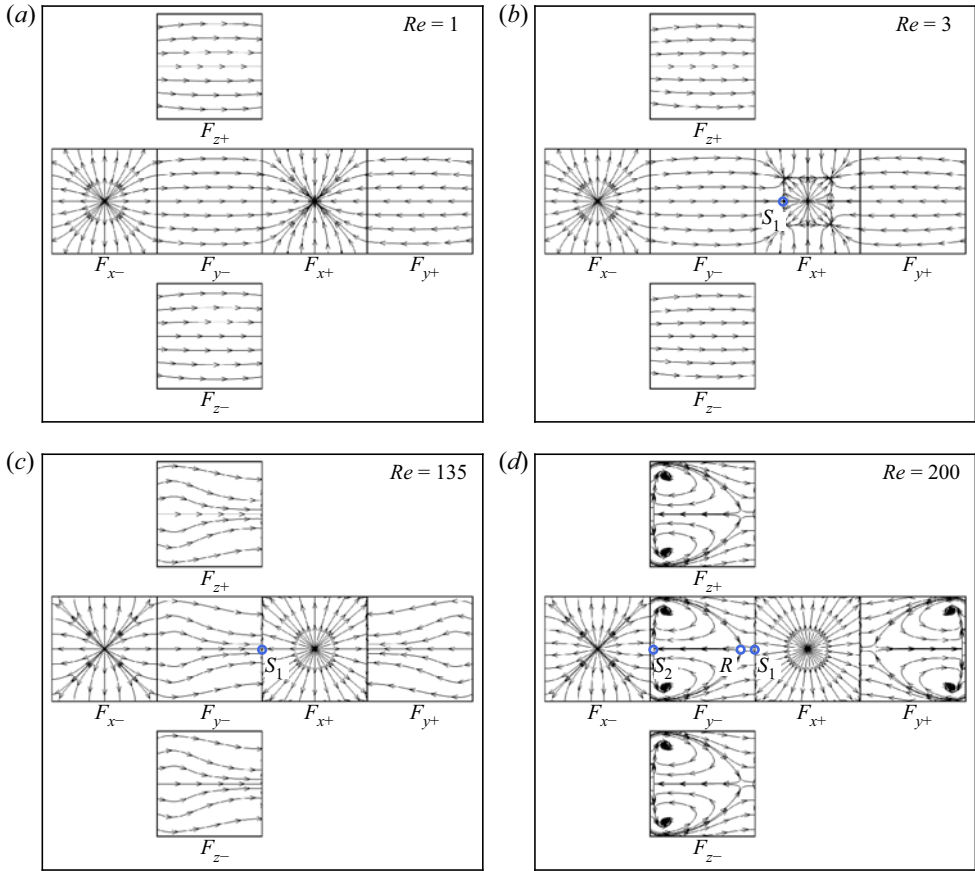


Figure 2. Two-dimensional streamlines on the cube faces, where (a) is for NS at  $Re = 1$ , (b) for OSS1 at  $Re = 3$ , (c) for OSS1 at  $Re = 135$  and (d) for OSS2 at  $Re = 200$ ;  $F_{x\pm}$ ,  $F_{y\pm}$  and  $F_{z\pm}$  denote cube faces in the corresponding directions implied by the subscripts;  $S_1$  and  $S_2$  denote the primary and secondary separation locations;  $R$  denotes the reattachment location.

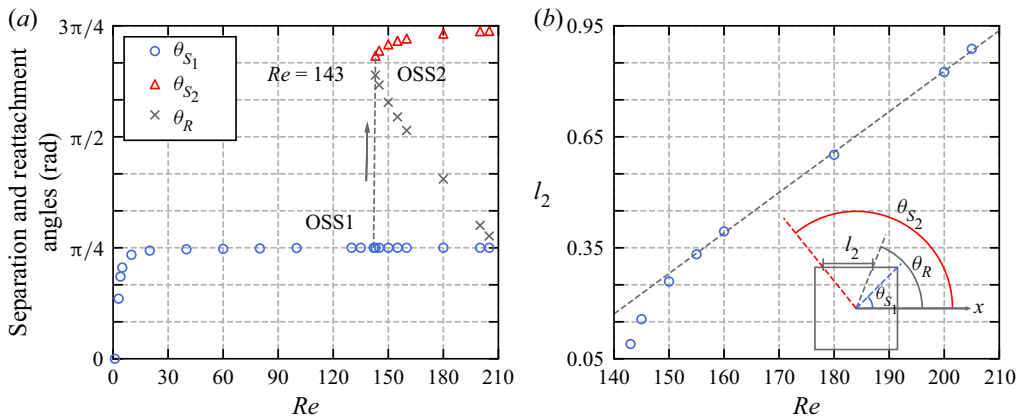


Figure 3. The separation and reattachment angles in the NS, OSS1 and OSS2 states as functions of  $Re$ .



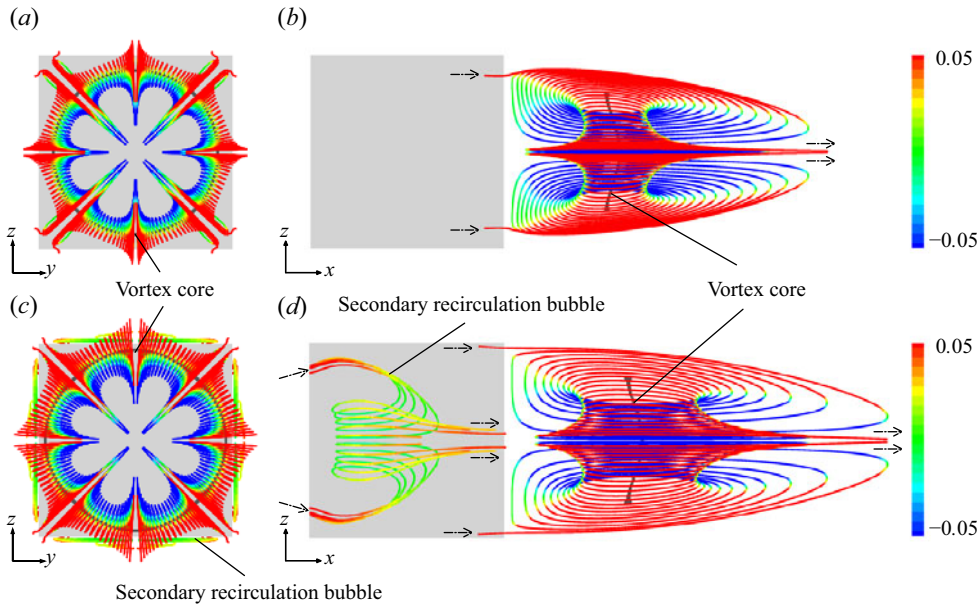


Figure 4. Vortex structure in the OSS1 and OSS2 states represented by three-dimensional steady streamlines coloured by the streamwise velocity  $u_x$ , where (a,b) are the rear and side views for OSS1 at  $Re = 135$ , while (c,d) are those for OSS2 at  $Re = 200$ ; the dash-dotted arrows in (b,d) show the entering and leaving of fluid particles along corresponding streamlines.

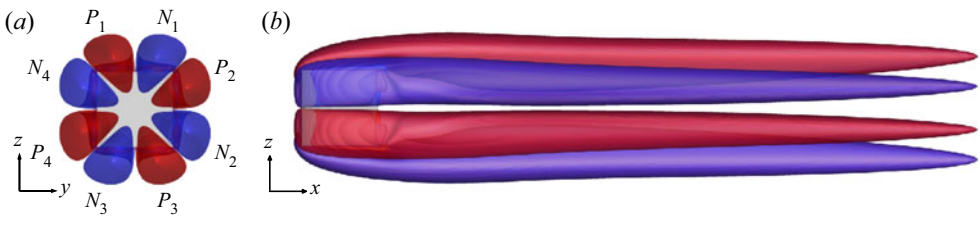


Figure 5. Steady vortex structure in the OSS regime depicted by the isosurface of  $\omega_x = \pm 0.03$  with red and blue for positive and negative values, respectively, where (a,b) are the rear and side views at  $Re = 200$ . The negative and positive streamwise vortex tubes are marked by  $N_i$  and  $P_i$  ( $i = 1, 2, 3$  and  $4$ ), respectively.

observed behind the cube. Four additional pairs of vortices are generated on the lateral faces of the cube for the OSS2 state at  $Re = 200$  in figures 4(c) and 4(d), forming the secondary recirculation bubbles. The typical flow structures are visualised by the isosurfaces of  $\omega_x = 0.03$  in red and  $\omega_x = -0.03$  in blue in figure 5. Four pairs of counter-rotating streamwise vortex tubes are also clearly observed, which are labelled by  $N_i$  for the negative ones and  $P_i$  for the positive ones ( $i = 1, 2, 3$  and  $4$ ) to facilitate further discussions.

4.2. Planar symmetry–steady flow

A regular bifurcation is observed at a  $Re$  value between 205 and 210, and the PSS regime is established in  $210 \leq Re \leq 250$ . The major difference between the OSS and PSS regimes lies in the spatial symmetry of the flow. Our results show that the rotational and reflection

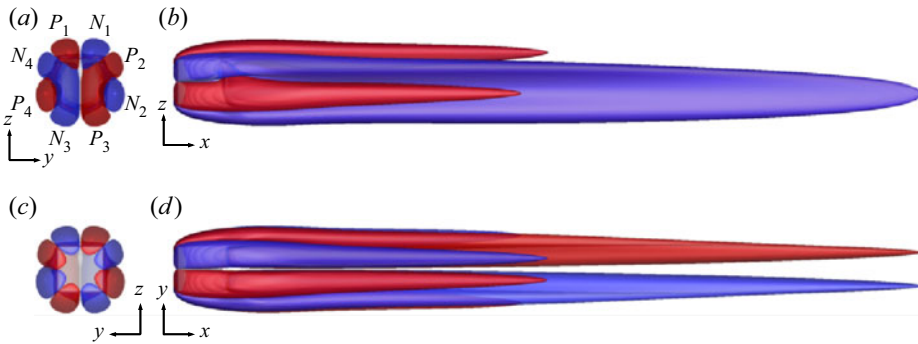


Figure 6. Isosurfaces of the streamwise vorticity  $\omega_x = \pm 0.03$  for the PSS regime at  $Re = 220$  with red and blue for positive and negative values, respectively. (a) Rear view, (b) side view against  $x-z$  plane, (c) front view and (d) side view against  $x-y$  plane. The negative and positive streamwise vortex tubes are marked by  $N_i$  and  $P_i$  ( $i = 1, 2, 3$  and  $4$ ), respectively.

symmetry conditions in (1.1)–(1.8) are broken and only one planar symmetry with respect to  $y = 0$ , i.e.  $\mathcal{G}_{y=0}^s$ , is retained.

The projected views for the isosurfaces of streamwise vorticity  $\omega_x = \pm 0.03$  are exhibited in figure 6. The rear and side views in figures 6(a), 6(b) and 6(d) show that two streamwise vortex tubes in the planar symmetry  $\mathcal{G}_{y=0}^s$  are generated by the merging of  $N_4$  with  $N_3$  and  $P_2$  with  $P_3$  in comparison with those labels marked in figure 5(a), forming a strong pair of vortex tubes that extend further downstream in the wake.

Figure 7 shows the transient variations of the lift coefficients  $C_{l,y}$  and  $C_{l,z}$  for the cases in the PSS regime. It is noted that for each case,  $C_{l,y}$  increases initially and then decreases to zero, while  $C_{l,z}$  increases and stabilises at a positive value. These evolution trends, corresponding to an observation that the flow develops from an unstable OSS state to PSS in the end, are the reflections of temporal development of the streamwise vortex tubes. To illustrate this evolution process, the merging processes of  $N_4$  with  $N_3$  and  $P_2$  with  $P_3$  are demonstrated in figure 8, where the rear views of isosurfaces  $\omega_x = \pm 0.03$  for the case  $Re = 220$  at different moments are plotted. The corresponding moments are marked in sequence as open circles on the time histories of both lift coefficients in figure 7. At the beginning  $t = 200$  in figure 7(a), the four pairs of streamwise vortex tubes are in orthogonal symmetry. As the instability develops,  $N_1$  and  $P_2$  are merged with  $N_4$  and  $P_3$ , respectively, as shown in figure 8(c) at  $t = 320$ . The wake structure becomes nearly symmetric with respect to the plane  $y = z$  at  $t = 320$ . Both of the two lift coefficients are increased in this process. In figures 8(c)–8(d) the combined structure by  $N_1$  with  $N_4$  continues to merge with  $N_3$ , and subsequently,  $N_1$  is split out from the combined structure of the three vortex tubes in figures 8(e)–8(g). The wake is thereby composed of two merged structures by  $N_4$  with  $N_3$  and  $P_2$  with  $P_3$ , along with four minor streamwise vortex tubes  $N_1, N_2, P_1$  and  $P_4$  in opposite signs. This form of wake keeps growing until it becomes fully planar symmetry with respect to the plane  $y = 0$ , as shown in figure 8(h). At this stage, the lift coefficient in the  $z$ -axis, i.e.  $C_{l,z}$ , is increased to a constant non-zero value, while  $C_{l,y}$  returns back to zero. This evolution process is dependent on initial perturbations, so that the PSS flow can also settle into state with symmetry about plane  $z = 0$ . It will be demonstrated in the next section that the merged vortex tubes play a significant role in initiating shedding of vortex tubes from the cube.

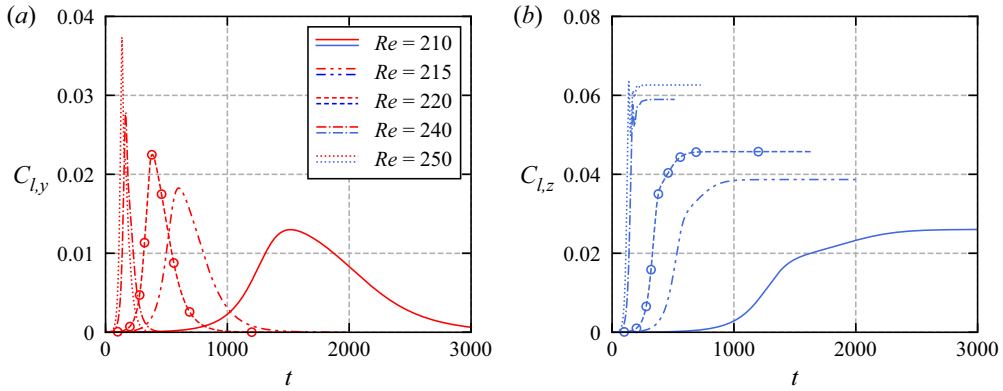


Figure 7. Time histories of  $C_{L,y}$  and  $C_{L,z}$  for all simulated cases in the PSS regime.

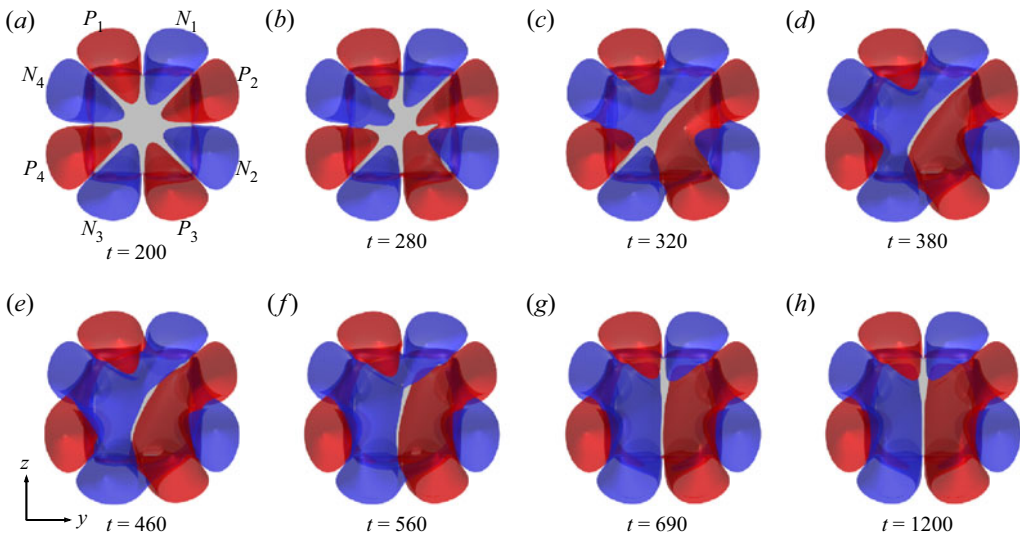


Figure 8. The merging process from the rear view between the streamwise vortex tubes characterised by the isosurface of  $\omega_x = \pm 0.03$  as the temporal growth for the PSS regime at  $Re = 220$ , where (a–h) correspond to the temporal moments marked by the open circles in figure 7. The negative and positive streamwise vortex tubes are labelled by  $N_i$  and  $P_i$  ( $i = 1, 2, 3$  and  $4$ ), respectively.

## 5. Unsteady flows

### 5.1. Evolution in phase space

The onset of HS by a Hopf bifurcation is observed at a critical  $Re$  value, denoted by  $Re_{cr}^{HT}$ , between 250 and 255. The focus of our investigation is on the characteristics and mechanism of vortex shedding. Three vortex shedding states are discovered in the HS regime, which are the regular, quasi-periodic and high-order synchronised shedding. As has been mentioned in § 3, these states will be referred to as HS1, QP and HS2, respectively, in the following discussions. Before we proceed to discuss the vortex shedding features in detail, the evolution in the phase space is first examined for the HS and CS regimes. Eight typical cases corresponding to flows from the onset of regular shedding to the disordered and irregular wake are considered through the frequency

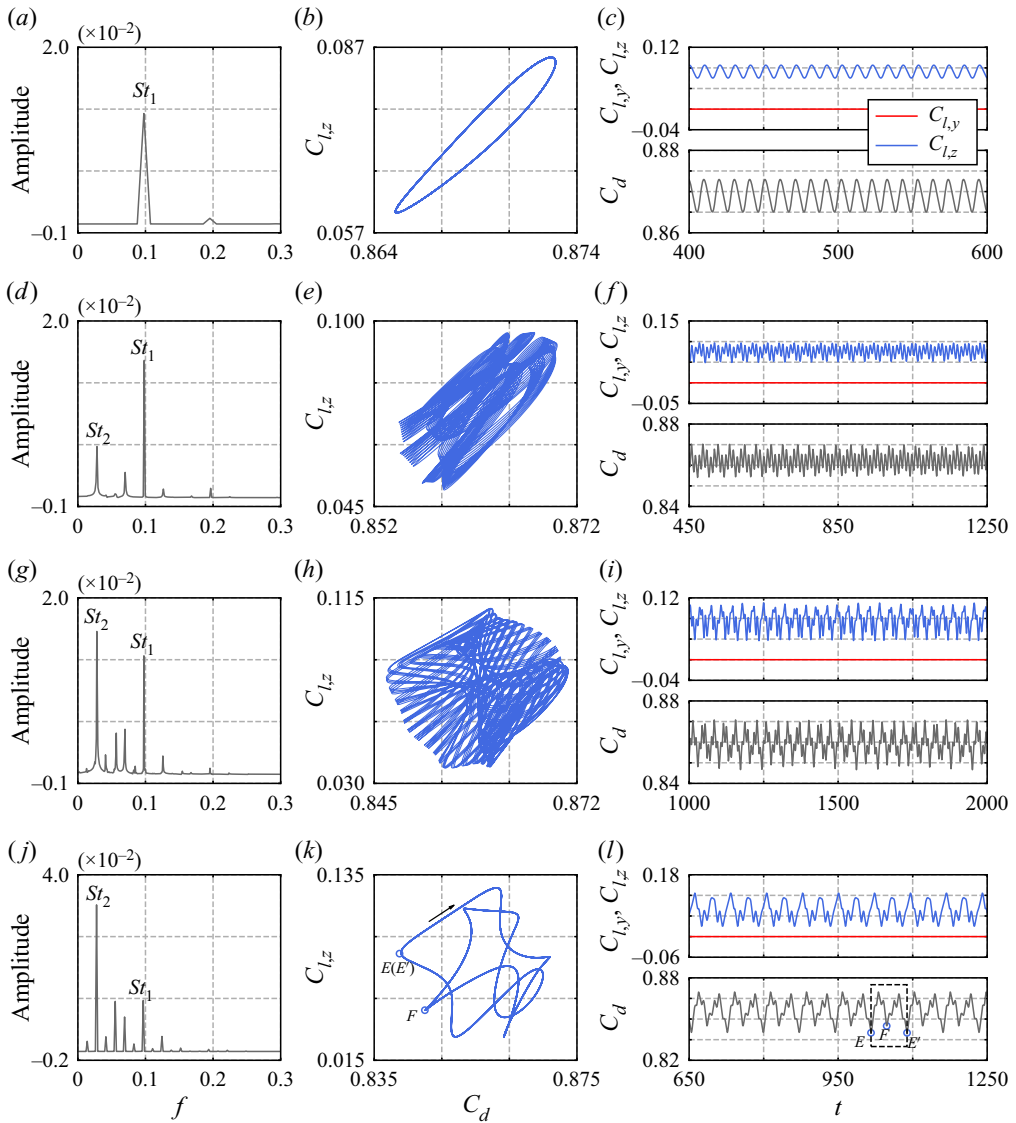


Figure 9. For caption see next page.

spectra and phase portraits based on the time histories of the drag and lift coefficients in **figure 9**. The Fourier spectrum is derived based on the temporal variation of  $C_{l,z}$ , where the non-dimensional frequency  $f$  is normalised by  $U$  and  $L$ , and, therefore, is equivalent to the Strouhal number.

For the HS1 state at  $Re = 270$ , which is slightly above  $Re_{cr}^{HT}$ , the single dominant frequency peak in **figure 9(a)**, the simple closed loop of phase portrait in **figure 9(b)** and the regular oscillations of  $C_{l,z}$  and  $C_d$  in **figure 9(c)** suggest that the vortex shedding is regular with  $St_1 \approx 0.0975$ .

As  $Re$  is increased beyond a critical value to  $Re = 282$ , the spectrum and phase portrait are featured by two dominant peaks and non-overlapping loops, respectively, signalling a transition of vortex shedding from HS1 to the QP state. The vortex shedding with

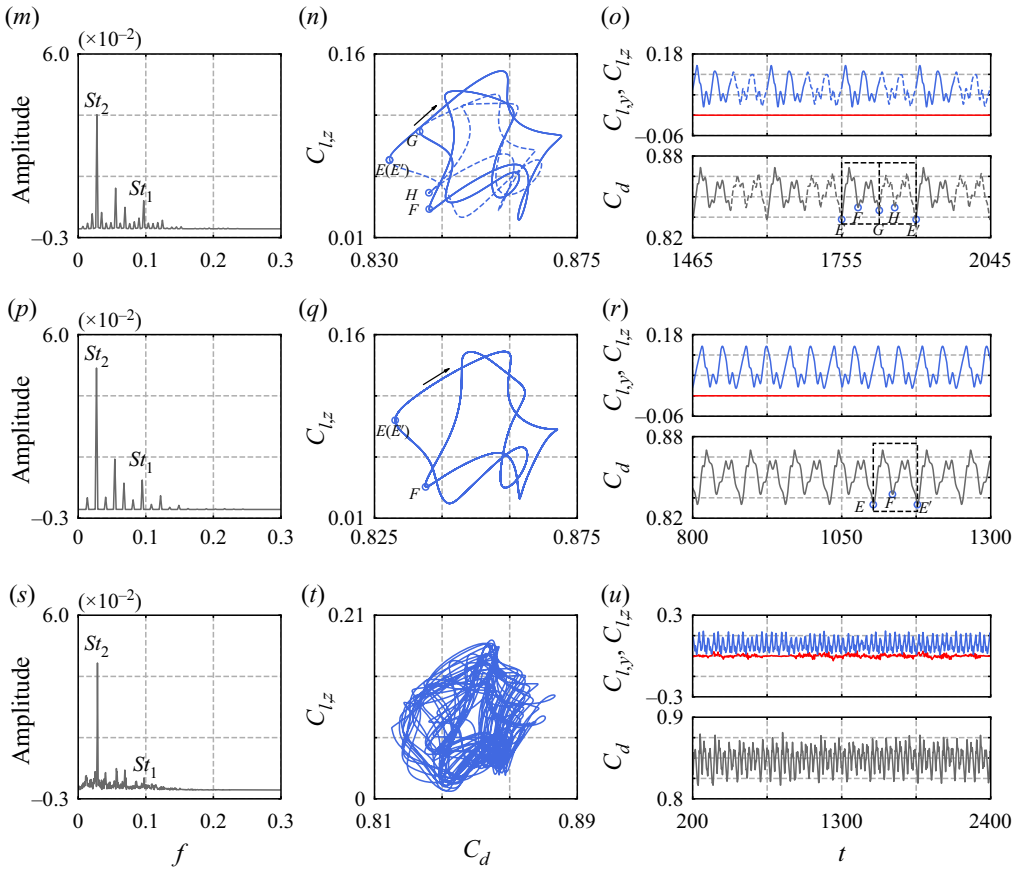


Figure 9 (cntd). Frequency spectra, phase portraits and time histories of the drag and lift coefficients with (a–c) for the HS1 state at  $Re = 270$ ; (d–f) and (g–i) for QP at  $Re = 282$  and  $285$ ; (j–l), (m–o) and (p–r) for HS2 at  $Re = 289, 295$  and  $300$ ; (s–u) for CS at  $Re = 315$ . The amplitudes of the frequency spectra are normalised by the signal length.

$St_1 \approx 0.0982$  is modulated by a low frequency component  $St_2 \approx 0.0281$ , suggesting the occurrence of a secondary instability in the flow. The low frequency component  $St_2$  becomes the dominant frequency in the spectrum at  $Re = 285$  as shown in figure 9(g), where  $St_1 \approx 0.0979$  and  $St_2 \approx 0.0280$ . To be consistent in the following discussions, we refer to  $St_1$  and  $St_2$  as vortex shedding and secondary frequencies, respectively. The quasi-periodic nature of the flow shown in the QP state suggests that  $St_1$  and  $St_2$  are incommensurable.

With a further increase of  $Re$  to  $Re = 289, 295$  and  $300$ , the flow transits to the HS2 state, where the phase portraits in figures 9(k), 9(n) and 9(q) return to immaculately overlapping patterns, demonstrating the restoration of periodicity and the synchronisation of flow modes with  $St_1$  and  $St_2$ . The interlaced loops of the phase portrait suggest the synchronisation is high order in those cases. A cascade of period-doubling and period-halving bifurcations is observed as  $Re$  increases from 289 to 300. Each full period of the time histories of  $C_d$  and  $C_{l,z}$  at  $Re = 295$  consists of four loops that can be grouped into two similar partitions, as marked by the two rectangles on the time history of  $C_d$  in figure 9(o). Five characteristic moments, denoted as  $E, F, G, H$  and  $E'$ , are selected to distinguish the four loops in the phase portrait, which are labelled as open circles in



figures 9(n) and 9(o). The four loops are thereby determined by the trajectory  $E \rightarrow F \rightarrow G \rightarrow H \rightarrow E'$  along the arrow direction in figure 9(n). The two similar partitions become identical to each other at  $Re = 289$  and  $300$ , demonstrating the period-doubling bifurcation from  $Re = 289$  to  $295$  and the period-halving bifurcation from  $Re = 295$  to  $300$ . The full periods for  $Re = 289$  and  $300$  are also marked by the rectangles in figures 9(l) and 9(r) with the selected characteristic moments  $E$ ,  $F$  and  $E'$ . As the results of the two bifurcations, the four loops of  $Re = 295$  are reduced into two loops, which are clearly represented by the trajectories  $E \rightarrow F \rightarrow E'$  in figures 9(k) and 9(q). The cascade of period-doubling and period-halving bifurcations is also observed in the wakes of other bluff bodies and different nonlinear dynamical systems (e.g. Cheng *et al.* 2020; Ju *et al.* 2020), which often signals the transition to chaos (Pikovsky, Rosenblum & Kurths 2003). The cascade of period doubling and period halving for the wake of the cube was detected by using  $\Delta Re = 1$ . We are uncertain if further cascading can be found by using smaller  $\Delta Re$ . The observation of  $C_{l,y} = 0$  in HS1, QP and HS2 suggests that the planar symmetry about  $y = 0$  is maintained in these states.

The chaotic vortex shedding is identified as a flow regime primarily because of the further breaking of symmetry about  $y = 0$  as  $Re \geq 310$ . A typical case at  $Re = 315$  is selected to exhibit the disordered and irregular nature of the flow in the CS regime. The appearance of small amplitude fluctuations of  $C_{l,y}$  in figure 9(u) marks the onset of flow instabilities associated with breaking of the planar symmetry with respect to  $y = 0$ . The dominance of  $C_{l,z}$  oscillations over  $C_{l,y}$  fluctuations suggests that the direction of vortex shedding at  $Re = 315$  largely remains in the  $x$ - $z$  plane, similar to those observed in the HS regime. The phase space of  $C_d$ - $C_{l,z}$  in figure 9(t) is characterised by non-overlapping irregular orbits, demonstrating the chaotic nature of the flow. While the low frequency  $St_2$  near  $f = 0.025$  remains dominant, the spectrum peak associated with  $St_1$  becomes weak such that it is hardly recognised, suggesting the regular vortex shedding associated with  $St_1$  is no longer a standout feature of the flow.

## 5.2. Periodic HS

### 5.2.1. Single-frequency shedding

The physical mechanism of the regular vortex shedding in the HS1 state is investigated first in order to understand the more complicated QP and HS2 states mentioned above. To this end, the development of flow structures for the case at  $Re = 270$  is examined at eight phases equally spaced in one period of vortex shedding, where  $St_1 \approx 0.0975$  and the period  $T_1 = 1/St_1 \approx 10.26$ . The corresponding temporal moments are marked by open circles and indexed by the  $i$  axis in figure 10(a). The initial attempts of identifying the vortex shedding mechanism were focused on the interactions of the major shear layers developed on the cube surface by visualising isosurfaces of  $\omega_y$  in the plane of  $y = 0$  and  $\omega_z$  in the plane of  $z = 0$  without much success, suggesting the mechanism of vortex shedding behind the cube is different from that around a circular cylinder (Griffin 1995). The focus is then shifted towards the isosurfaces of  $\omega_x$  as shown in figure 11, where  $\omega_x = 0.1$  and  $\omega_x = -0.1$  are marked by red and blue, respectively. This shift of focus is prompted by the observation that the near-wake structures are dominated by the streamwise vortex tubes, as demonstrated in figures 5 and 6 for the OSS and PSS regimes, respectively. Given the flow is symmetric about  $y = 0$ , the computational domain is divided into two halves and only the wake structure in the region of  $y < 0$  is exhibited. Each of the frames in figure 11 corresponds to one of the eight temporal moments shown in figure 10(a), and consists of two projection views of the isosurfaces in the half-domain  $y < 0$ . The left column represents the  $x$ - $z$  views of the streamwise vortex tubes towards the negative direction



Wake transitions behind a cube in  $Re$  1–400

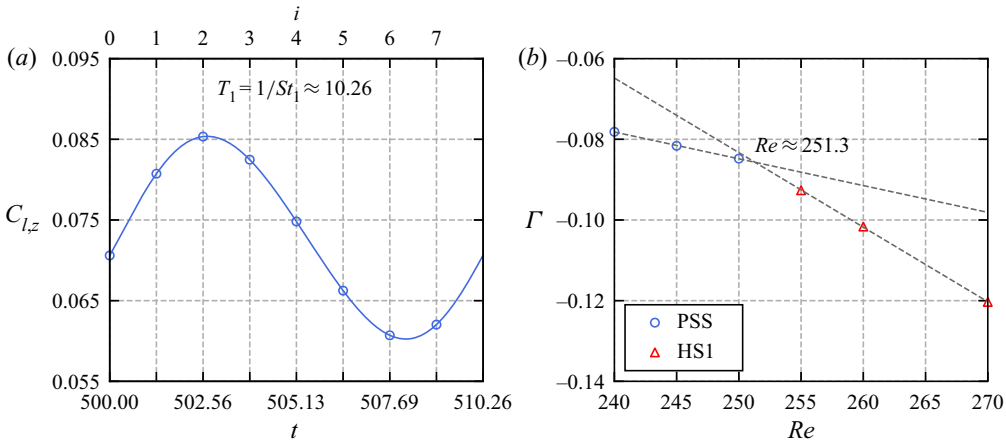


Figure 10. (a) Time history of  $C_{l,z}$  in a single period at  $Re = 270$  in the HS1 state, where the secondary axis  $i$  is employed to denote the selected eight temporal moments extracted by  $\Delta t = T_1/8$ . (b) The circulation of the negative streamwise vortex tube  $\Gamma$  in the vicinity of Hopf transition. For the definition of circulation, see the discussion.

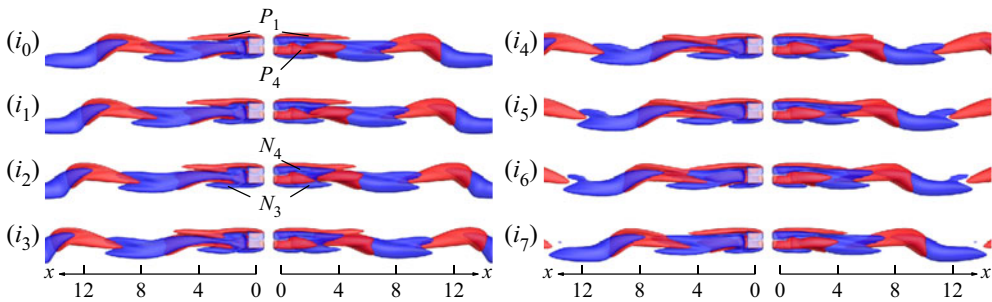


Figure 11. Isosurfaces of the streamwise vorticity with  $\omega_x = 0.1$  as red and  $\omega_x = -0.1$  as blue for the HS1 state at  $Re = 270$ , where  $(i_0)–(i_7)$  correspond to the temporal moments marked in figure 10(a). The same wake structure in the region of  $y < 0$  is plotted as two views in each frame, in which the left and the right ones are about the  $x–z$  view along the negative and positive  $y$ -axis, respectively. The streamwise vortex tubes in the  $y < 0$  region are labelled as  $N_3$ ,  $N_4$ ,  $P_1$  and  $P_4$  in  $(i_0)$  and  $(i_2)$ .

of the  $y$ -axis, while the right column is the  $x–z$  views of the same structure towards the positive direction of the  $y$ -axis. The streamwise directions are marked by the  $x$ -axes for the left and right columns. In this way, the interaction between the opposite-sign vortex tubes can be observed from both directions.

It is reasonable to anticipate that, near the critical  $Re$  for the Hopf bifurcation, the wake instability is evolved from a steady structure similar to the one shown in figure 6. To be consistent, the labels  $P_1$ ,  $P_4$ ,  $N_4$  and  $N_3$  are again employed to mark the tubes in figure 11( $i_0$ ) and 11( $i_2$ ). The strength of the streamwise vortex tubes is expected to increase with increasing  $Re$ . In order to substantiate this inference, the circulation  $\Gamma$  is quantified by integrating the time-averaged streamwise vorticity over the region  $\{x = 6, -2 \leq y \leq 0, -2 \leq z \leq 2\}$ . The circulation contained in a slice of the vortex tube is chosen to represent the circulation contained in the tube is primarily because it is not straightforward to calculate the circulation in the three-dimensional vortex tube. Nonetheless, we find this representation works quite well, as evidenced by the variation trend of  $\Gamma$  with  $Re$  in the

vicinity of Hopf bifurcation shown in [figure 10\(b\)](#). The cut-off value of  $\omega_x > -0.0001$  is used to quantify the circulation of the negative streamwise vortex tubes. It is seen from [figure 10\(b\)](#) that the strength of the negative vortex tube (i.e. the absolute value of  $\Gamma$ ) indeed increases with  $Re$  as we inferred. The different variation trends of  $\Gamma$  in the PSS and HS regimes allow us to determine the critical  $Re$  for Hopf bifurcation as the intersection of the two variation trends. The critical  $Re$  of 251.3 estimated here is very close to the value of 252.0 determined through Landau's equation to be presented later on in [§ 6.2](#).

When  $Re > Re_{cr}^{HT}$ , the merged tube by  $N_4$  with  $N_3$  in the domain  $y < 0$  is incapable of sustaining more circulation, since the vorticity is continuously fed into it from the cube surface. The excessive amount of circulation is accumulated at the downstream end of the merged tube by  $N_4$  with  $N_3$ , forming a section of strong negative vortex tube in  $5 < x < 8$ , as shown in [figure 11\(i<sub>0</sub>\)](#). The low pressure induced by the section of the strong negative vortex tube tends to draw  $P_1$  and  $P_4$  towards it, leading to a merging process by  $P_1$  with  $P_4$  from [figure 11\(i<sub>0</sub>\)](#) to [11\(i<sub>4</sub>\)](#). As the merged tube by  $P_1$  with  $P_4$  gains significant strength, it will cut into the merged tube by  $N_4$  with  $N_3$  and eventually leads to the shedding of the section of the strong negative vortex tube in [figure 11\(i<sub>5</sub>\)](#). The vorticity continues to accumulate in the downstream end of the merged tube by  $P_1$  with  $P_4$ . The low pressure region induced by merged  $P_1$  with  $P_4$  encourages the merging of  $N_4$  with  $N_3$ , which eventually cuts off the strong positive section of the merged tube by  $P_1$  with  $P_4$  and leads to its shedding, as shown in [figure 11\(i<sub>6</sub>\)](#) and [11\(i<sub>7</sub>\)](#). Then a full vortex shedding cycle is finished. In summary, the regular vortex shedding in the HS1 state is characterised by a process involving the merging, cutting-off and releasing of  $N_4$  with  $N_3$  and  $P_1$  with  $P_4$  in the region  $y < 0$ . The same process in the region  $y > 0$  can be also described by those of  $P_2$  with  $P_3$  and  $N_1$  with  $N_2$ . The physical mechanism behind this process is that the low pressure induced by the strong section of merged streamwise vortex tubes attracts another two streamwise vortex tubes of opposite signs towards it, and the subsequent merging of the two opposite-sign vortex tubes leads to the shedding of the strong section of merged streamwise vortex tubes. This process happens alternately in two halves of a regular shedding period.

The wake structure at  $Re = 270$  is further illustrated by the isosurface of  $\lambda_2$  in [figure 12](#) (for  $\lambda_2$  technique, see Jeong & Hussain 1995), where the isosurfaces are coloured by the streamwise vorticity  $-0.03 < \omega_x < 0.03$  varying from blue to red. The flow at the moment  $i = 7$  in [figure 10\(a\)](#) is only employed to plot the global view in [figure 12\(a\)](#), since the length of the compute domain is enough to display the propagation of hairpin vortices in three full periods, so that the evolution of a hairpin vortex can be approximately traced by comparing these consecutive cycles. The complex interactions of vortex tubes in the wake lead to the unique wake structures observed in [figure 12\(a\)](#), which are distinctly different from those formed in the wake of long cylindrical structures such as circular cylinders and prisms of different cross-section shapes (Thompson *et al.* 2006; Sau 2009). The shedding process characterised by the merging and cutting-off of streamwise vortex tubes in [figure 11](#) forms upper and lower branches for the hairpin vortices in the wake, as marked in [figure 12\(a\)](#). From the near-wake view in [figure 12\(b\)](#), the streamwise vortex tubes can also be clearly distinguished from the isocontour of  $\lambda_2$  around the cube, where only the positive tubes  $P_1$  and  $P_4$ , and the negative ones  $N_1$  and  $N_2$  are marked accordingly. Further discussions on the dynamics and evolution of the hairpin vortices are not presented here, because it digresses from the topic of this study, while it might be a worthwhile point to form a separated investigation in the future.

## Wake transitions behind a cube in $Re$ 1–400

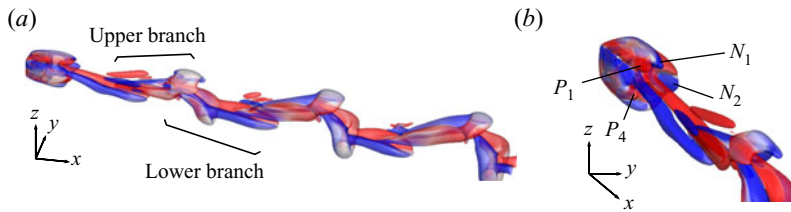


Figure 12. Representation of the wake structure at  $Re = 270$  by isosurfaces of  $\lambda_2$  coloured by a blue-white-red colour map of  $\omega_x$  varying from  $-0.03$  to  $0.03$ , where (a,b) are the global and near-wake structures at the moment  $i = 7$  in figure 10(a).

### 5.2.2. Quasi-periodic shedding

The QP state is characterised by the emergence of a dominant low frequency component ( $St_2$ ) that modulates the regular oscillations of the lift coefficient observed in the HS1 state. Although the QP state has not been reported before for the laminar wake of a cube, similar phenomena involving modulating frequencies have been found in other bluff-body flows, e.g. Lee (2000) and Tomboulides & Orszag (2000) for spheres; Gao *et al.* (2018) for an inclined circular disk; Bohorquez *et al.* (2011) for a slender blunt-based body. The physical origin of  $St_2$  along with the shedding of hairpin vortices for the cube is considered by taking advantage of the QP state at  $Re = 282$ , where  $St_1 \approx 0.0982$  remains dominant over  $St_2 \approx 0.0282$ , as shown in figure 9(d). It is noted that  $St_1/St_2 \sim 7/2$ , corresponding to the occurrence of seven vortex shedding cycles in approximately two secondary periods. This behaviour suggests the state observed here is in the vicinity of a high-order synchronisation of  $St_1/St_2 = 7/2$  in the parameter space, where the ratio of two frequencies is a rational number (Pikovsky *et al.* 2003). Previous studies (e.g. Ren *et al.* 2019) have shown that the stroboscopic view of flow fields sampled at the higher frequency over the entire period of the low frequency constitutes an effective way of revealing the physical mechanism of quasi-periodic oscillation. The regular vortex shedding frequency  $St_1 \approx 0.0982$  is used as the sampling frequency over the secondary period in the following flow visualisations.

Figure 13(a) exhibits the time history of  $C_{l,z}$  for the case  $Re = 282$ , where eight temporal moments, as marked by the open circles, are uniformly distributed in time under  $\Delta t = 1/St_1 \approx 10.18$ . The secondary axis  $i$  is employed to refer to each moment. It is seen that the phases of the open circles are not identical and  $C_{l,z}$  oscillates around a mean value over the secondary period, confirming the quasi-periodic nature of the flow. The projected  $x$ - $z$  views of the flow field sampled at those moments are shown in figure 14, where the vortex structure is represented by the isosurface of  $\lambda_2$  coloured by the streamwise vorticity  $-0.03 < \omega_x < 0.03$ . A remarkable flow feature observed in figure 14 is that the phase at which the head of the lower branch is released into the wake becomes unstable and varies from cycle to cycle, underlying the occurrence of a secondary instability. The phase undergoes two oscillation cycles over seven vortex shedding periods from figures 14( $i_0$ ) to 14( $i_7$ ), corresponding to  $St_1/St_2 \sim 7/2$ . This observation allows us to conclude that  $St_2$  is induced by a secondary instability associated with temporal evolution of the wake structure behind the cube. The geometry of the hairpin vortices in the wake of  $Re = 282$  is similar to that of  $Re = 270$  in figure 12 since  $St_1$  is still dominant, while the relatively weak streamwise oscillation by  $St_2$  can also be observed as the propagation of the coherent structures in the same magnitude as shown for the release of the heads in figure 14. Identification of the physical origin of this secondary instability based on the flow features at this Reynolds number is not straightforward because the

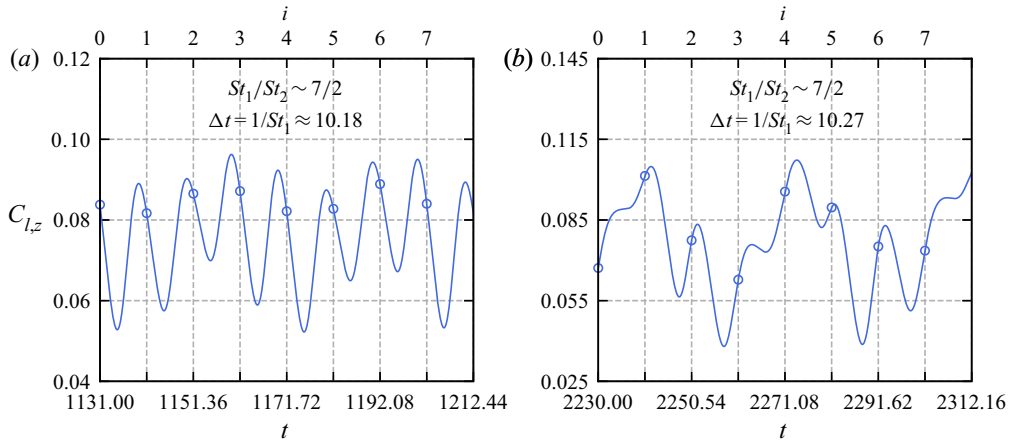


Figure 13. Selected ranges of time histories of  $C_{l,z}$  for the QP state at (a)  $Re = 282$  and (b)  $Re = 285$ , where the eight moments under  $\Delta t = 1/St_1 \approx 10.18$  for  $Re = 282$  and the other eight ones under  $\Delta t = 1/St_1 \approx 10.27$  for  $Re = 285$  are marked with open circles and can be referred to by the secondary axis  $i$ .

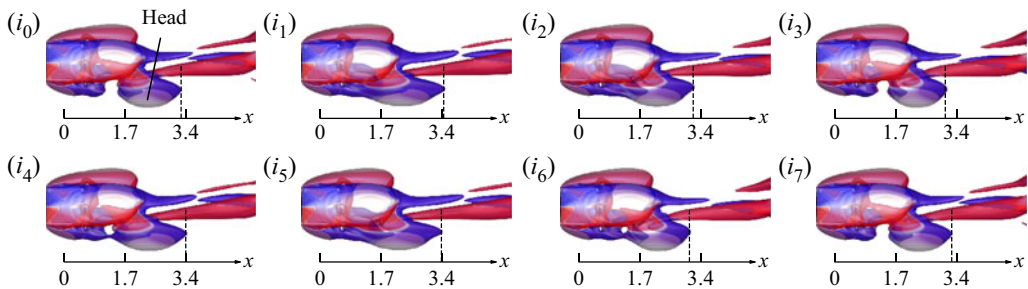


Figure 14. Stroboscopic plots for the case at  $Re = 282$  in the QP state, with  $St_1 \approx 0.0982$  as the sampling frequency. The near-wake region is characterised by the  $x$ - $z$  views of the isosurface of  $\lambda_2$  in a blue-white-red colour map of  $\omega_x$  varying from  $-0.03$  to  $0.03$ , and  $(i_0)$ – $(i_7)$  correspond to the moments by the open circles in figure 13(a).

secondary oscillation is relatively weak. We will continue exploring the physical origin of the secondary instability through more numerical examples below.

An interesting phenomenon is observed between  $Re = 282$  and  $285$ . The secondary frequency  $St_2$  becomes the dominant frequency component at  $Re = 285$  and this dominance over  $St_1$  continues to grow with increasing  $Re$  thereafter. This observation suggests the secondary instability associated with  $St_2$  has become the dominant feature of flow around a cube at  $Re \geq 285$ . To explore the flow feature associated with  $St_2$ , the stroboscopic plots of the isosurface of streamwise vorticity in the space of  $y < 0$ , at selected moments marked in figure 13(b), are examined in figure 15. The oscillation of  $C_{l,z}$  sampled at the vortex shedding frequency  $St_1$  becomes more pronounced than that shown in figure 13(a), which is consistent with the contrast between the wake structure observed in figures 14 and 15. The wake structures at different moments shown in figure 14 would have been identical if there were not secondary frequency  $St_2$ . The different wake structures observed in figure 15 are induced by the phase oscillation of the vortex shedding process observed in figure 11. The oscillation of the wake structure can be clearly observed if our focus is placed on the structure enclosed by the dashed rectangle in figure 15( $i_0$ ).

### Wake transitions behind a cube in $Re$ 1–400

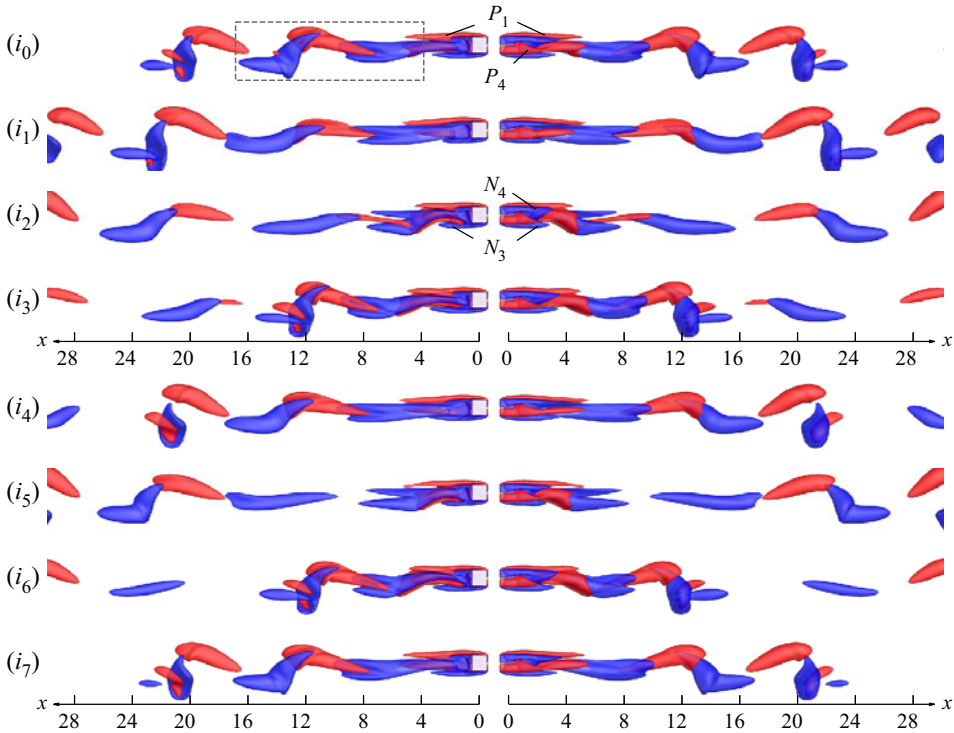


Figure 15. Stroboscopic plots for the case at  $Re = 285$  in the QP state, with  $St_1 \approx 0.0979$  as the sampling frequency. The isosurfaces of  $\omega_x = 0.1$  as red and  $\omega_x = -0.1$  as blue are presented in the same way as figure 11, where  $(i_0)$ – $(i_7)$  correspond to the temporal moments marked in figure 13(b).

The positive and negative vortex tubes in  $8 < x < 16$  start to lower down horizontally in the next two vortex shedding periods, before curling to a similar posture to that shown in figure 15( $i_0$ ) at a moment between figures 15( $i_3$ ) and 15( $i_4$ ), completing a cycle of wake oscillation in  $St_2$ .

The above oscillation process repeats again approximately from figures 15( $i_4$ ) to 15( $i_7$ ), completing two cycles of wake oscillation within approximately seven periods of vortex shedding. The near-wake structure shown in figure 15 shows an excellent correlation to the phase oscillation of  $C_{l,z}$  sampled at the vortex shedding frequency  $St_1$  in figure 13(b) with  $St_1/St_2 \sim 7/2$ .

#### 5.2.3. High-order synchronised shedding

As  $Re$  is further increased, the flow changes from the QP state to the HS2 state which occurs over  $289 \leq Re \leq 305$ . One of the unique characteristics in the HS2 state is that  $St_1/St_2 = 7/2$ , suggesting a high-order synchronisation between flow features associated with  $St_1$  and  $St_2$ . The underlying physics behind the  $7/2$  synchronisation is that seven cycles of vortex shedding happen exactly over two secondary periods.

The time history of  $C_{l,z}$  in two typical secondary periods  $2T_2 = 2/St_2 \approx 73.86$  is shown in figure 16 for  $Re = 300$ . For the purpose of flow visualisation, the two secondary periods are divided into two uneven periods with  $T_1 \approx 40.49$  and  $T_2 \approx 33.37$  based on the recurrence pattern of the lift coefficient  $C_{l,z}$ . The flow structures are visualised through the isosurfaces of  $\omega_x$  in figure 17. In each of  $T_1$  and  $T_2$ , 16 moments are selected uniformly,



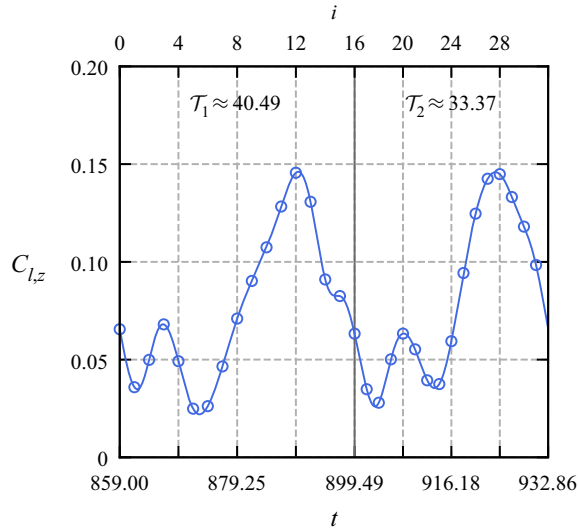


Figure 16. Time history of  $C_{l,z}$  in two secondary periods  $2T_2 = T_1 + T_2$  for the HS2 state at  $Re = 300$ . The full period  $2T_2$  is divided into two portions  $T_1 \approx 40.49$  and  $T_2 \approx 33.37$  by the recurrence of  $C_{l,z}$ , where 16 moments are uniformly selected for each portion, as marked by the open circles. The secondary axis  $i$  is employed to refer to every moment.

as shown by the open circles in figure 16. All of the moments are plotted for the isosurfaces of  $\omega_x$  in figure 17. There are more snapshots of the flow field employed in figure 17 than those shown in previous cases so as to identify the physics behind the secondary oscillation of the wake. The visualisation method employed in figure 17 is the same as that used in figure 11 at  $Re = 270$ .

The alternate shedding process of vortex tubes at the initial phases of  $T_1$  is similar to that observed in HS1, as shown by the flow features corresponding to  $St_1$  in figure 11. Three pairs of vortex tubes, whose negative and positive branches are marked as  $V_1$ ,  $V_2$  and  $V_3$ , are shed into the wake from figures 17( $i_0$ ) to 17( $i_9$ ). The flow becomes rather stable after that and only one pair of vortex tubes, marked as  $V_4$ , is shed between the moments spanning from figures 17( $i_9$ ) to 17( $i_{15}$ ), forming a large peak of  $C_{l,z}$  spanning from  $i = 9$  to 15 in figure 16. Regular vortex shedding resumes after that with two pairs of vortex tubes  $V_5$  and  $V_6$  shed from figures 17( $i_{16}$ ) to 17( $i_{23}$ ), where the positive branch of  $V_4$  is squeezed together with the shedding of  $V_5$  in figure 17( $i_{16}$ ). The flow becomes stable again with only one pair of vortex tubes  $V_7$  shed between the moments spanning from figures 17( $i_{23}$ ) to 17( $i_{31}$ ), forming another large peak of  $C_{l,z}$  between  $i = 23$  and  $i = 31$  in figure 16. It is clear from the above observation that the dominant flow feature associated with  $St_2$  is the two relatively stable flow cycles over exactly seven periods of vortex shedding at  $St_1$ .

The interaction of streamwise vortex tubes appears to be responsible for the relatively stable flow cycles. The vortex tubes  $N_4$ ,  $N_3$ ,  $P_1$  and  $P_4$  become relatively weak in figure 17( $i_9$ ) after the consecutive shedding of three pairs of vortex tubes in figures 17( $i_0$ )–17( $i_9$ ), and experience an epoch of growth after figure 17( $i_9$ ). Subsequently, the fast growth of merged  $N_4$  and  $N_3$  hinders the growth and merging of  $P_1$  and  $P_4$  through the cancellation mechanism of vorticity of opposite signs, leading to a substantial delay of the shedding of the merged  $N_4$  and  $N_3$  in figure 17( $i_{14}$ ). The delayed shedding process observed at the second half of  $T_2$  is due to the same flow mechanism described above.

The oscillation of the primary recirculation zone for  $Re = 300$  is examined through the streamlines on the plane  $y = 0$ , as shown in figure 18, where the even values of  $i$  in



Wake transitions behind a cube in  $Re$  1–400

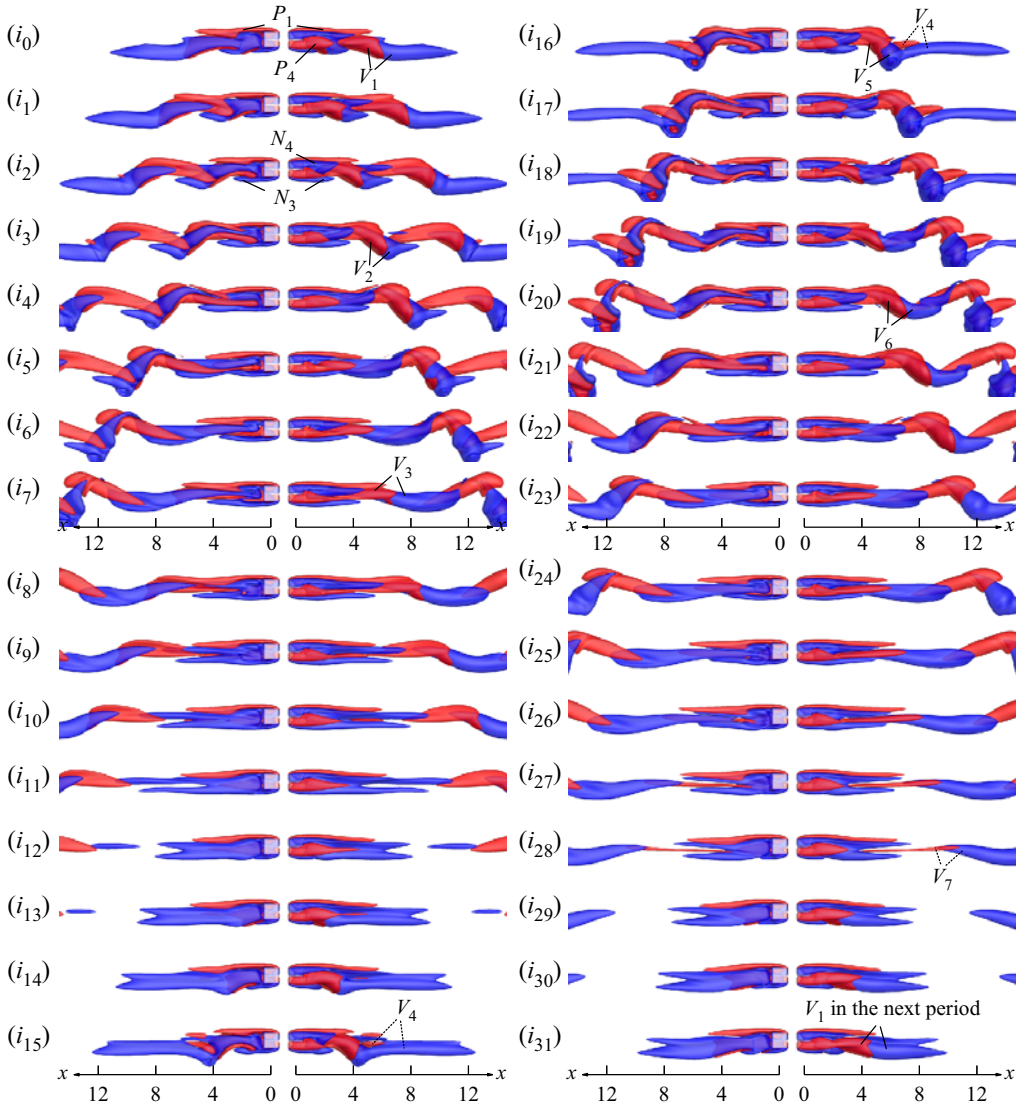


Figure 17. Isosurfaces of the streamwise vorticity with  $\omega_x = 0.1$  as red and  $\omega_x = -0.1$  as blue for the HS2 state at  $Re = 300$ , where  $(i_0)$ – $(i_{15})$  correspond to the first 16 temporal moments marked within  $\mathcal{T}_1$  in figure 16, while  $(i_{16})$ – $(i_{31})$  correspond to the rest of the 16 moments in  $\mathcal{T}_2$ . The manner to exhibit the flow structures in figure 11 is employed.

figure 16 are plotted. It is noted that the upper side of the recirculation zone is sustaining during the full shedding period, while the lower side oscillates under the spectrum of the high-order synchronised state, which is similar to the motion of streamlines in the HS1 flow (e.g. figure 18 of Saha 2004 and figure 5 of Klotz *et al.* 2014).

5.3. Chaotic shedding

That the flow becomes chaotic has been shown with the case  $Re = 315$  in figures 9(s)–9(u). As  $Re$  is further increased, larger amplitude fluctuations will occur both on  $C_{l,y}$  and  $C_{l,z}$ ,

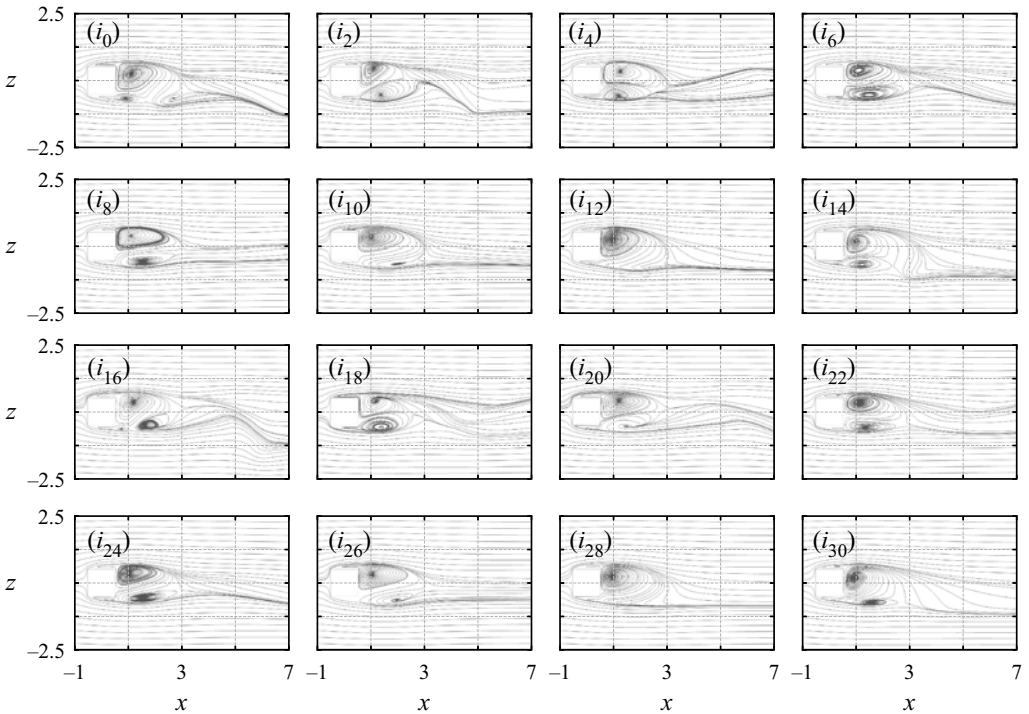


Figure 18. The periodic variations of the two-dimensional streamlines on the plane  $y = 0$  at  $Re = 300$  in the HS2 state, where the moments at even values of  $i$  in figure 16 are exhibited in each plot.

suggesting the dominant shedding direction switches in the  $y$ - $z$  plane. To facilitate further discussions, temporal variations of  $C_{l,y}$  and  $C_{l,z}$  at  $Re = 390$  are examined over three intervals marked by the dashed rectangles in figures 19(a) and 19(b). In the first and second intervals, one of the lift coefficients oscillates around a non-zero value while the other one oscillates around zero, indicating the vortex shedding is in either the  $x$ - $z$  or  $x$ - $y$  plane. It is interesting to note that both of the lift coefficients oscillate around non-zero values in the third interval, where  $C_{l,y}$  oscillates around a positive value while  $C_{l,z}$  around a negative one. It is speculated that the primary direction of vortex shedding is in the  $y = -z$  plane during this interval. To confirm this speculation, the lift coefficients in the third interval are recalculated by projecting to the diagonal directions, i.e.  $\hat{C}_{l,y} = \sqrt{2}/2(C_{l,y} - C_{l,z})$  and  $\hat{C}_{l,z} = \sqrt{2}/2(C_{l,y} + C_{l,z})$ . The original and transformed lift coefficients are plotted in figures 19(c) and 19(d). We note that the mean values of the original  $C_{l,y}$  and  $C_{l,z}$ , i.e. 0.069 and  $-0.085$ , are close to each other in magnitude and both away from zero in figure 19(c), while the transformed  $\hat{C}_{l,z}$  decreases to a value around zero in figure 19(d). This result basically confirms the above speculation. Since the flow shedding remains nearly in the plane  $y = -z$  only briefly, we suspect the flow is relatively unstable on the diagonal planes of  $y = z$  and  $y = -z$ .

To further confirm the above inference, the coherent structures represented by isosurfaces of  $\lambda_2$  are exhibited in figure 20, where the hairpin vortices are plotted at three selected moments  $t = 600, 1247$  and  $2101$  from the three intervals. Figures 20(a,c,e) and 20(b,d,f) show the  $x$ - $y$  and  $x$ - $z$  projected views, respectively. It is clearly observed, in figures 20(a) and 20(b) at  $t = 600$ , that the vortex shedding mainly occurs in the  $z$  direction. While, it changes to the  $y$  direction in figures 20(c) and 20(d) for  $t = 1247$ , and becomes oblique in figures 20(e) and 20(f) for  $t = 2101$ .

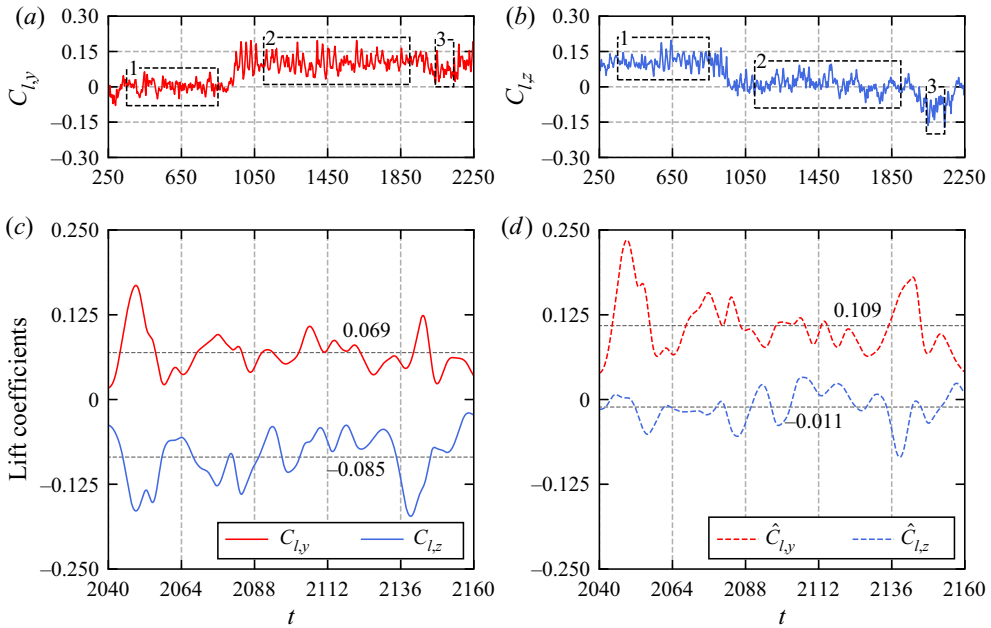


Figure 19. Time histories of lift coefficients for the case at  $Re = 390$ , where (a,b) are  $C_{l,y}$  and  $C_{l,z}$  with three distinct intervals marked by the rectangles, (c) is the two lift coefficients in the third interval, and (d) is the lift coefficients by mapping onto the diagonal direction through  $\hat{C}_{l,y} = \sqrt{2}/2(C_{l,y} - C_{l,z})$  and  $\hat{C}_{l,z} = \sqrt{2}/2(C_{l,y} + C_{l,z})$ .

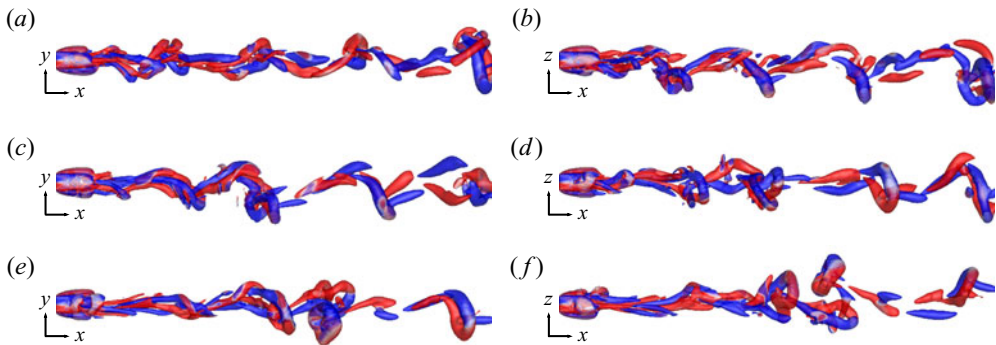


Figure 20. Isosurfaces of  $\lambda_2$  at  $Re = 390$  coloured by the streamwise vorticity  $-0.03 < \omega_x < 0.03$  varying from blue to red, where (a,b) are projected views of the coherent structure on the  $x$ - $y$  and  $x$ - $z$  planes for  $t = 600$ , (c,d) are for  $t = 1247$  and (e,f) are for  $t = 2101$ .

## 6. Weakly nonlinear instability analysis

### 6.1. Regular bifurcation

The nature of the regular and Hopf bifurcations observed in the wake of a cube is investigated through weakly nonlinear analysis in this section. The regular bifurcation from OSS to PSS is a stationary one between two steady states and is believed to be a pitchfork bifurcation, which was also mentioned as a supercritical imperfect bifurcation in Klotz *et al.* (2014). The trajectories of the regular bifurcation in the wake of the

cube are bijectively reflected by the growth of the lift coefficients exerted on the cube, as exhibited in figures 7 and 8. The non-dimensional lift force can be characterised by the two-dimensional vector  $(C_{l,y}, C_{l,z})$ , which will be disturbed from its equilibria in the vicinity of flow transition from OSS to PSS. Thus, a two-dimensional dynamical system regarding the variation of the  $(C_{l,y}, C_{l,z})$  can be employed to describe the regular bifurcation as follows:

$$\frac{dC_{l,y}}{dt} = f(C_{l,y}, C_{l,z}), \tag{6.1}$$

$$\frac{dC_{l,z}}{dt} = f(C_{l,z}, C_{l,y}). \tag{6.2}$$

The orthogonal symmetry of the flow demonstrates that  $(C_{l,y}, C_{l,z}) = (0, 0)$  is the only stable fixed point in the OSS regime before it bifurcates to the PSS regime, where the planar symmetry with respect to the plane either  $y = 0$  or  $z = 0$  is retained. Due to the symmetry of the cube with respect to the diagonal direction,  $C_{l,y}$  and  $C_{l,z}$  are interchangeable, which guarantees an identical  $f(\xi, \eta)$  in (6.1) and (6.2). Four equilibria at  $(\pm C_l^{sat}, 0)$  and  $(0, \pm C_l^{sat})$ , where  $C_l^{sat}$  denotes the  $\ell^2$ -norm of the lift coefficients at saturation, are expected based on (6.1) and (6.2). The form of the coupling terms in  $f(\xi, \eta)$  can be determined through Taylor expansion at  $(0, 0)$  and enforcing symmetry conditions of  $(C_{l,y}, C_{l,z}) \rightarrow (-C_{l,y}, C_{l,z})$  and  $(C_{l,y}, C_{l,z}) \rightarrow (C_{l,y}, -C_{l,z})$ ,

$$f(\xi, \eta) = k_1\xi + k_2\xi^3 + k_3\xi\eta^2 + \dots, \tag{6.3}$$

where  $k_1, k_2$  and  $k_3$  are real coefficients and, as to each term  $\xi^m\eta^n$ ,  $m + n$  is odd and  $n$  has to be even.

Substituting (6.3) into (6.1) and (6.2) and omitting high-order terms, we have

$$\frac{dC_{l,y}}{dt} = C_{l,y}[k_1 + k_2(C_{l,y}^2 + \gamma C_{l,z}^2)], \tag{6.4}$$

$$\frac{dC_{l,z}}{dt} = C_{l,z}[k_1 + k_2(C_{l,z}^2 + \gamma C_{l,y}^2)], \tag{6.5}$$

where  $\gamma = k_3/k_2$ . Eight non-trivial equilibria for  $(C_{l,y}, C_{l,z})$  can be obtained from (6.4) and (6.5),

$$\left(\pm\sqrt{-\frac{k_1}{k_2}}, 0\right), \left(0, \pm\sqrt{-\frac{k_1}{k_2}}\right), \tag{6.6}$$

$$\left(\pm\sqrt{-\frac{k_1}{k_2(1+\gamma)}}, \pm\sqrt{-\frac{k_1}{k_2(1+\gamma)}}\right), \left(\pm\sqrt{-\frac{k_1}{k_2(1+\gamma)}}, \mp\sqrt{-\frac{k_1}{k_2(1+\gamma)}}\right). \tag{6.7}$$

The stability of the coupled pitchfork system at these equilibria can be further examined by linear stability analysis. By applying the variational operation to (6.4) and (6.5), the corresponding Jacobian matrix can be derived as

$$J(C_{l,y}, C_{l,z}) = \begin{pmatrix} k_1 + k_2(3C_{l,y}^2 + \gamma C_{l,z}^2) & 2\gamma k_2 C_{l,y} C_{l,z} \\ 2\gamma k_2 C_{l,z} C_{l,y} & k_1 + k_2(3C_{l,z}^2 + \gamma C_{l,y}^2) \end{pmatrix}. \tag{6.8}$$

The equilibrium  $(0, 0)$  is known as unstable in PSS. Therefore, the eigenvalues of  $J(0, 0)$  denoted as  $\lambda_{1,2} = k_1$  should be positive, i.e.  $k_1 > 0$ . Without loss of generality, we take

$(0, \sqrt{-k_1/k_2})$  as the fixed point  $(0, C_l^{sat})$ . It is thus required that  $k_2 < 0$  and the eigenvalues of  $J(0, \sqrt{-k_1/k_2})$  derived as  $\lambda_1 = -2k_1$  and  $\lambda_2 = k_1(1 - \gamma)$  are both negative, which results in  $\gamma > 1$ . The determinate signs of  $k_2$  and  $\gamma$  imply that the third-order nonlinear terms stabilise the coupled pitchfork bifurcation system and the nature of the regular transition in the wake of the cube is supercritical. Through the same reasoning, the stability of the diagonal equilibria in (6.7) can be shown as saddle points, suggesting the existence of the alternative PSS regime with respect to the diagonals are impossible in the wake of the cube.

The time histories of  $C_{l,y}$  and  $C_{l,z}$  at  $Re = 210$ , which is slightly above the critical  $Re$  value of the bifurcation from OSS to PSS, are plotted in figure 21(a) to quantify the value of  $k_2$ . The linear forms of (6.4) and (6.5) can be written as

$$\frac{d \ln C_{l,y}}{dt} = k_1 + k_2(C_{l,y}^2 + \gamma C_{l,z}^2), \tag{6.9}$$

$$\frac{d \ln C_{l,z}}{dt} = k_1 + k_2(C_{l,z}^2 + \gamma C_{l,y}^2). \tag{6.10}$$

The dependence of  $(d \ln C_{l,y}/dt)$  on  $(C_{l,y}^2 + \gamma C_{l,z}^2)$  and  $(d \ln C_{l,z}/dt)$  on  $(C_{l,z}^2 + \gamma C_{l,y}^2)$  is tested by assuming different values of  $\gamma$  in (6.9) and (6.10) and the corresponding results are plotted in figures 21(b) and 21(c). Both equations become approximately linear at  $\gamma \approx 1.435$ , which leads to  $k_1 \approx 0.00572$  and  $k_2 \approx -8.43$  deduced via linear fitting.

With this set of control parameters at  $Re = 210$ , the predictions of time histories of  $(C_{l,y}, C_{l,z})$  based on (6.4) and (6.5) with an initial perturbation of  $(0.835, 1.07) \times 10^{-5}$  are plotted in figure 21(a), and the possible trajectories in phase space  $C_{l,y}$ – $C_{l,z}$  is demonstrated in figure 21(d). The predictions based on the two-dimensional coupled pitchfork model are in good agreement with the simulation results. The four stable fixed points located on the axes and the four saddle nodes on the diagonals are clearly observed through those trajectories.

The supercritical nature of the bifurcation from OSS to PSS implies that any infinitesimal disturbances will initiate the flow bifurcation from OSS to PSS when the Reynolds number is slightly greater than the critical value. Thus, the critical value of Reynolds number for the regular transition, denoted as  $Re_{cr}^{RT}$ , can be estimated as the point where the linear growth rate  $k_1$  changes its sign. Figure 22 illustrates the linear initial stage of  $\ln C_l$  for four cases in the vicinity of the regular transition and the dependence of the growth rate on  $Re$ . The critical value of  $Re_{cr}^{RT} \approx 207.0$  is obtained through a linear correlation of the growth rate with  $Re$ .

### 6.2. Hopf bifurcation

The nature of the Hopf bifurcation from PSS to HS1 is considered below. At the onset of the HS1 state, a pair of complex eigenvalues should emerge to govern the growth of disturbance, for which Landau’s equation has been proven appropriate to describe this nonlinear dynamical behaviour (Stuart 1960; Watson 1960) as

$$\frac{dZ}{dt} = c_1 Z + c_2 |Z|^2 Z + \dots, \tag{6.11}$$

where  $Z = |Z|e^{i\phi}$  represents the complex disturbance of interest, with  $|Z|$  and  $\phi$  being its amplitude and phase, respectively;  $c_i = a_i + ib_i$  is the complex coefficient. In particular,  $a_2$  is the first Lyapunov coefficient.

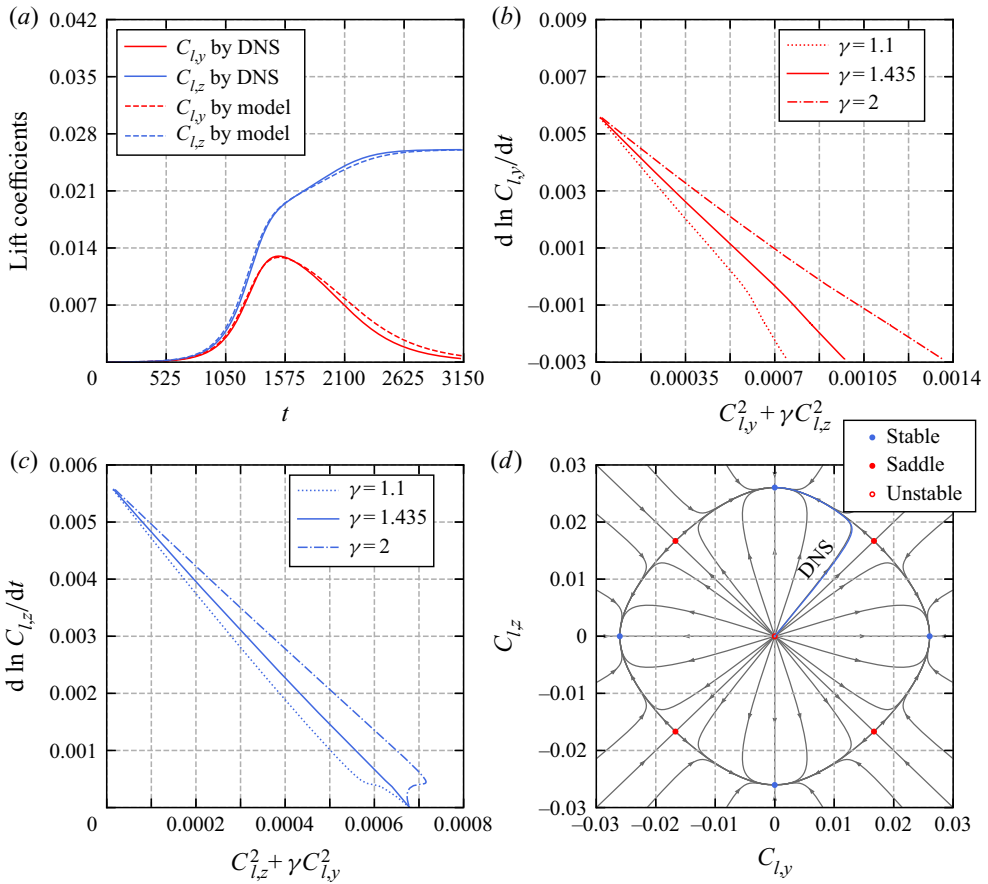


Figure 21. (a) Time histories of  $C_{l,y}$  and  $C_{l,z}$  either by the DNS results at  $Re = 210$  or by the prediction of the coupled pitchfork bifurcation model; (b) the linear dependence of  $(d \ln C_{l,y}/dt)$  on  $(C_{l,y}^2 + \gamma C_{l,z}^2)$ ; (c) the linear dependence of  $(d \ln C_{l,z}/dt)$  on  $(C_{l,z}^2 + \gamma C_{l,y}^2)$ ; (d) the trajectories with stable, saddle and unstable equilibria of the coupled pitchfork model in the phase space.

Substituting the expression of  $Z$  into (6.11), the temporal variation of the amplitude and phase are decoupled, such that we obtain an equation with respect to  $|Z|$  in the form of

$$\frac{d \ln |Z|}{dt} = a_1 + a_2 |Z|^2 + \dots \quad (6.12)$$

With the similar criterion to the pitchfork bifurcation, the nature of the Hopf bifurcation can be determined by the sign of the first Lyapunov coefficient  $a_2$ . Figure 23(a) shows the time histories of the lift coefficients at  $Re = 255$ , which is slightly greater than the critical value  $Re$  for the Hopf bifurcation. The two characteristic dynamical behaviours displayed by the time histories of the lift coefficients, namely the rapid decay of  $C_{l,y}$  to zero and the growth of  $C_{l,z}$  to a periodic pattern for  $t > 300$ , are somewhat expected. The rapid decay of  $C_{l,y}$  to zero suggests the flow symmetry about the plane  $y = 0$  is retained in HS1, while the growth of  $C_{l,z}$  to the periodic pattern implies that the regular vortex shedding occurs in the  $x-z$  plane. Based on the results shown in figure 23(a), the time history of  $C_{l,z}$  for  $t > 300$  is selected for the consideration of Landau's equation, and the amplitude is extracted by



Wake transitions behind a cube in  $Re$  1–400

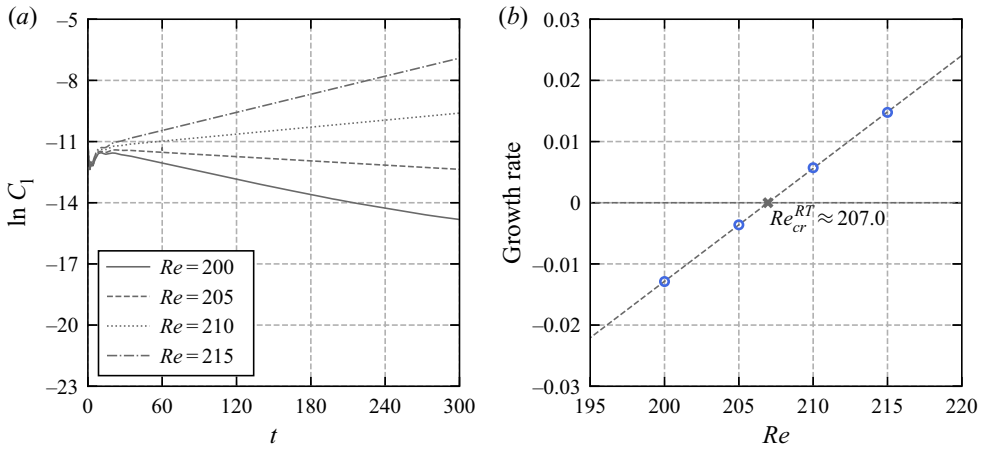


Figure 22. (a) Time histories of  $\ln C_l$  at  $Re = 200$  and  $205$  for the OSS2 state and  $Re = 210$  and  $215$  for the PSS state; (b) the linear relation regarding the growth rate of  $C_l$  as the increase of Reynolds number, where the critical Reynolds number for the regular transition  $Re_{cr}^{RT}$  is estimated at  $207.0$  by interpolation.

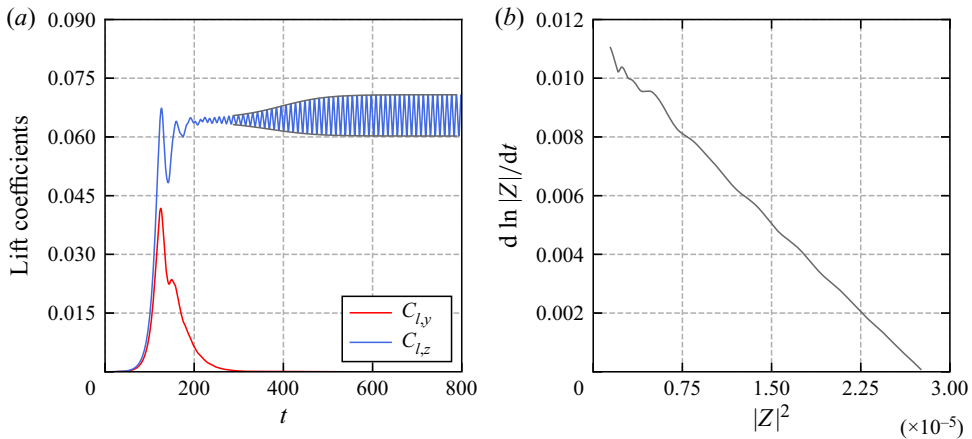


Figure 23. (a) Time histories of  $C_{l,y}$  and  $C_{l,z}$  with the employed upper and lower envelopes at  $Re = 255$ ; (b) the linear correlation between  $d \ln |Z|/dt$  and  $|Z|^2$ .

means of

$$|Z| = \frac{\text{upper envelope} - \text{lower envelope}}{2}. \quad (6.13)$$

The relation between  $d \ln |Z|/dt$  and  $|Z|^2$  is calculated in figure 23(b), in which a linear dependence is subsequently established with a negative slope, such that the sign of  $a_2$  is recognised. Therefore, the Hopf bifurcation is determined as supercritical, which is consistent with Klotz *et al.* (2014), and the wakes of a sphere (Thompson, Leweke & Provansal 2001) and ring tori (Sheard, Thompson & Hourigan 2004).

The critical Reynolds number for the transition from PSS to HS1, denoted as  $Re_{cr}^{HT}$ , is estimated by correlating the growth rate with  $Re$  in the vicinity of the transition point from  $Re = 245$  to  $255$ . For the cases with  $Re < Re_{cr}^{HT}$ , artificial perturbations are introduced

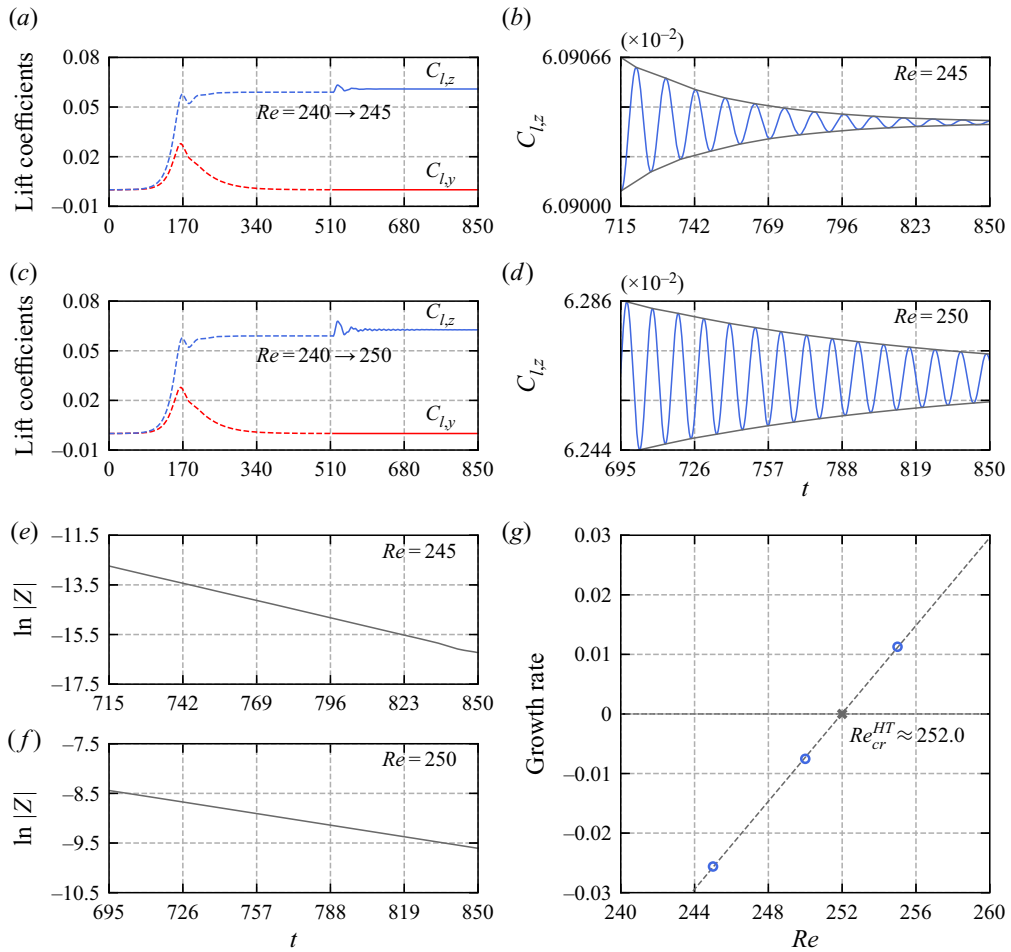


Figure 24. Linear interpolation for the critical Reynolds number of Hopf transition: (a–d) the time histories of lift coefficients for  $Re = 245$  and  $250$  obtained by using  $Re = 240$  at  $t = 516$  as the initial flow state; (e, f) are the linear relations between the amplitude  $\ln |Z|$  and  $t$ ; (g) the growth rates for cases in the vicinity of the Hopf transition, where the critical value  $Re_{cr}^{HT}$  is estimated at  $252.0$  by interpolation.

to disturb the flows at  $Re = 245$  and  $250$  in order to obtain the growth rate. The steady solution of the flow at  $Re = 240$  is used as the initial condition for the simulations at  $Re = 245$  and  $250$ . The envelopes employed to calculate the growth rate at  $Re = 245$  are exhibited in figures 24(a) and 24(b), and those for  $Re = 250$  are in figures 24(c) and 24(d). The amplitude of each envelope  $|Z|$  is derived by the same expression in (6.13), and the variations of  $\ln |Z|$  against  $t$  are plotted in figures 24(e) and 24(f) for  $Re = 245$  and  $250$ , respectively. A linear correlation shown in figure 24(g) suggests  $Re_{cr}^{HT} \approx 252.0$ .

### 6.3. Global bifurcation features

Global bifurcation features of flow around a cube are examined by plotting peak values of  $C_{l,y}$  and  $C_{l,z}$  in figure 25 over the range of  $Re$  investigated in the present study. Since the peak values of  $C_{l,y}$  and  $C_{l,z}$  are extracted from temporal variations of  $C_{l,y}$  and  $C_{l,z}$

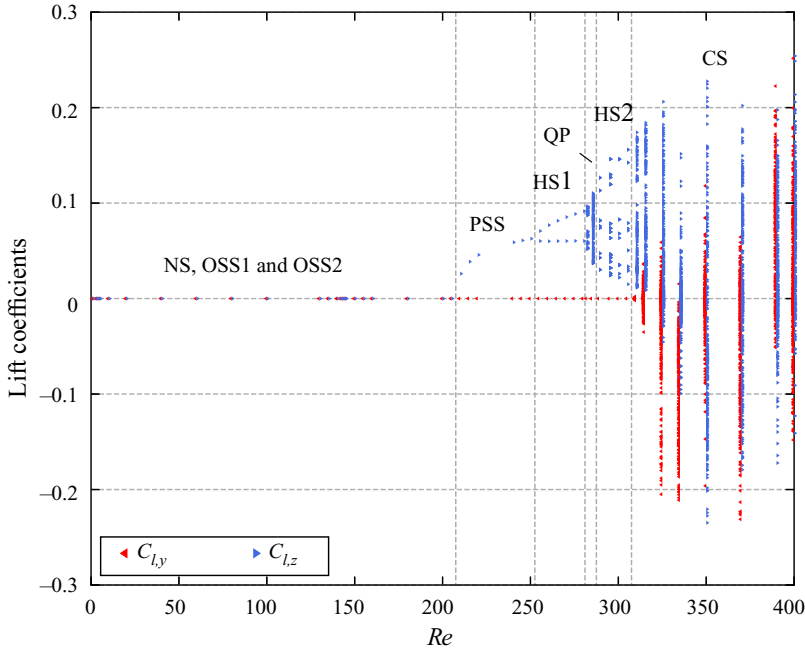


Figure 25. Bifurcation diagram by the stable orbits of the lift coefficients in all recognised flow states and regimes.

over a long period of simulation time (at least five periods for  $255 \leq Re \leq 305$  and 1500 time units for  $310 \leq Re \leq 400$ ), [figure 25](#) actually represents a phase diagram in  $Re$  space. The global bifurcation is characterised by different types of attractors. In the OSS regime, which includes the NS, OSS1 and OSS2 states, the attractors are fixed points at  $(C_{l,y}, C_{l,z}) = (0, 0)$ . The attractor is a fixed point at  $(0, C_{l,z})$  in the PSS regime. In the HS1 state the time history of  $C_{l,z}$  starts to oscillate between two local extrema periodically. Therefore, the stable orbit of  $C_{l,z}$  settles into a limit circle with a non-zero mean of  $C_{l,z}$ . The limit circle of  $C_{l,z}$  is distorted by the emerging secondary instability in the QP state. The two branches of local maxima and minima are scattered into inconsistent values. With the periodicity re-established in the form of high-order synchronisations in the HS2 state, the dispersed characteristic values of  $C_{l,z}$  return to a finite number of consistent values again, corresponding to that the limit torus collapses to well-defined limit circles in the HS2 state. The cascade of period-doubling and period-halving bifurcations is qualitatively reflected on the number of local maxima and minima of  $C_{l,z}$  at different Reynolds numbers. In the CS regime the flow is governed by chaotic attractors, such that both  $C_{l,y}$  and  $C_{l,z}$  start to oscillate randomly with the breaking of planar symmetry with respect to the  $y = 0$  plane.

The evolution of the mean drag coefficient  $\overline{C_d}$ , the length of the primary recirculation zone  $l_1$  and the Strouhal numbers  $St_1$  and  $St_2$  with  $Re$  are illustrated in [figures 26\(a\)](#), [26\(b\)](#) and [26\(c\)](#), respectively. The mean drag coefficient  $\overline{C_d}$  experiences a monotonic decrease with increasing  $Re$  until  $Re \approx 310$ , which coincides with the onset of the CS regime. In the CS regime,  $\overline{C_d}$  increases slightly with increasing  $Re$ . This trend of  $\overline{C_d}$  against  $Re$  is apparently different with that of freely moving cubes, where  $\overline{C_d}$  will first decrease as the drag coefficient of the fixed cube in lower Reynolds numbers and then experience a sudden increase approximately at  $Re = 150\text{--}200$  (e.g. Haider & Levenspiel 1989; Tran-Cong,

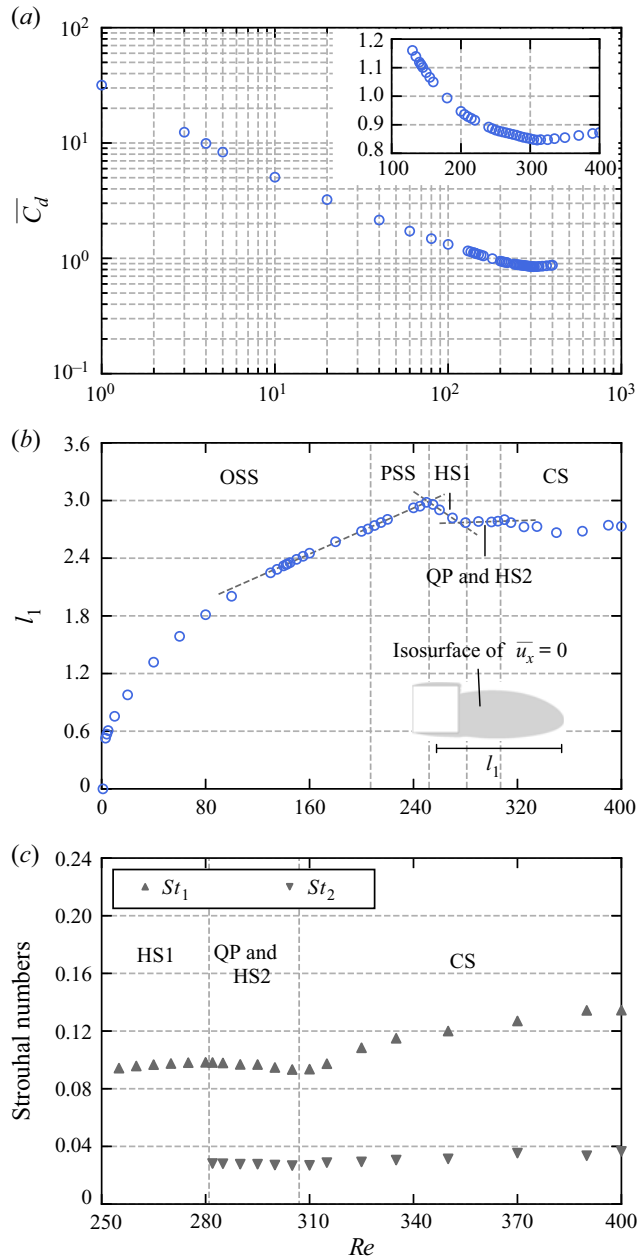


Figure 26. (a) The time-averaged drag coefficients  $\overline{C_d}$  against  $Re$ ; (b) the length of the primary recirculation zone  $l_1$  against  $Re$ , where  $l_1$  is defined by the maximal  $x$  coordinate on the isosurface of  $\overline{u_x} = 0$ ; (c) the Strouhal numbers  $St_1$  and  $St_2$  against  $Re$  in the unsteady regimes.

Gay & Michaelides 2004; Seyed-Ahmadi & Wachs 2019). This is because additional degrees of freedom for the cube leads to a wake transition into helical settling trajectories (Seyed-Ahmadi & Wachs 2019). The length of the primary recirculation zone  $l_1$ , defined by the maximal  $x$  coordinate on the isosurface of  $\overline{u_x} = 0$ , is employed to characterise the mean size of the vortex bubble behind the cube. This definition is equivalent to that by

Klotz *et al.* (2014), where the distance from the centre of the cube to the location of the streamwise velocity changing its sign was defined as  $l_1$ . The  $l_1$  variation illustrated in figure 26(b) shows a monotonic increasing trend until the onset of Hopf bifurcation at  $Re_{cr}^{HT} \approx 252.0$ , a linearly decreasing trend in the HS1 state over  $255 \leq Re \leq 280$ , a near constant value in the QP and HS2 states over  $282 \leq Re \leq 305$ , and an irregular variation trend in the CS regime for  $310 \leq Re \leq 400$ . The Strouhal numbers shown in figure 26(c), due to the strong spectral leakage in the CS regime, are calculated based on the streamwise velocity at  $(3, 0, 0)$  and represented by the largest values among multiple peaks around  $f = 0.1$  for  $St_1$  and  $f = 0.025$  for  $St_2$ . It is noted that the values of  $St_1$  and  $St_2$  are both slightly increased in HS1 but exhibit decreasing trends in QP and HS2. However, in the CS regime for  $310 \leq Re \leq 400$ ,  $St_1$  and  $St_2$  turn to be obviously increasing against  $Re$ .

## 7. Conclusion

Steady approaching flow around an isolated cube is investigated numerically through DNS over the range of Reynolds number 1–400 in this study. The canonical situation, where the streamwise direction is perpendicular to a face of the cube, is taken into consideration. High-resolution simulations with small increments of Reynolds numbers are employed in order to precisely determine the important flow features. The conclusions drawn from the study are summarised below.

- (i) A number of flow regimes are identified over  $Re$  1–400, including the orthogonal symmetry–steady (OSS,  $Re \leq 205$ ), planar symmetry–steady (PSS,  $210 \leq Re \leq 250$ ), hairpin-vortex shedding (HS,  $255 \leq Re \leq 305$ ) and chaotic vortex shedding (CS,  $Re \geq 310$ ) regimes in the sequence of increasing Reynolds number. The transitions among these regimes are characterised, in sequence, by the change from orthogonal symmetry to planar symmetry, a Hopf bifurcation, and the breaking of periodicity and all symmetry conditions, accordingly.
- (ii) The orthogonal symmetry formed by four pairs of steady streamwise vortex tubes in the wake of the cube is one of the profound flow features in the OSS regime. Three flow states are further identified in the OSS regime based on the features of flow separation on the cube surface. The flow separation is first detected on the rear face of the cube at  $Re = 3$  and remains on the rear face until  $Re$  is increased to a value between 142 and 143, marking the end of the OSS1 state. The flow separates and reattaches on the side faces of the cube, and separates again on the edges of the rear face for  $143 \leq Re \leq 205$ , which is denoted as the OSS2 state.
- (iii) A flow bifurcation from OSS flow to a PSS flow about  $y = 0$  occurs as the Reynolds number is increased beyond 205, leading to the formation of the PSS flow regime. The profound feature of the PSS flow is the merging of like-sign streamwise vortex tubes on either side of  $y = 0$ , forming a strong pair of opposite-sign streamwise vortex tubes in the wake of the cube. The weakly nonlinear stability analysis conducted in the present study, through constructing two coupled amplitude equations based on pitchfork bifurcations, confirms that the bifurcation from OSS to PSS is supercritical, where four stable fixed points on the  $y = 0$  and  $z = 0$  planes, and four saddle points on the  $y = z$  and  $y = -z$  planes are established. The critical Reynolds number for the regular transition is estimated at 207.0 by interpolation for the linear growth rates.
- (iv) The supercritical Hopf bifurcation to the HS regime is determined to take place at  $Re_{cr}^{HT} \approx 252.0$  through Landau's equation. The HS regime is comprised of the regular (HS1), quasi-periodic (QP) and high-order synchronised (HS2) vortex

shedding states. In the vicinity of the critical Reynolds number for the HS regime, the vortex shedding is regular with a well-defined Strouhal number  $St_1$ . As the Reynolds number is increased beyond a critical value around  $Re = 282$ , vortex shedding becomes quasi-periodic where the temporal variation of the lift coefficient is modulated by a secondary low frequency component of  $St_2$ . The spectrum peak corresponding to the secondary frequency  $St_2$  becomes dominant at  $Re = 285$  of the QP state. As  $Re$  is further increased to  $Re = 289$ , 295 and 300, the flow transits to the HS2 state, which is characterised by high-order synchronisations. A cascade of period-doubling and period-halving bifurcations is observed among these cases. The phase portraits of the cases at  $Re = 289$  and  $Re = 300$  are comprised of two well-defined interlaced loops, whereas four loops are observed in the phase portrait at  $Re = 295$ . The cascade of period-doubling and period-halving bifurcations observed in the present study is similar to those observed in other nonlinear dynamical systems and bluff-body flows, and is believed to be a precursor to the transition to the CS regime.

- (v) The regular vortex shedding in the HS1 state is induced by the interaction of merged streamwise vortex tubes in the wake. Two pairs of merged vortex tubes of opposite signs are shed in turn and cut off each other in a period of vortex shedding.
- (vi) The quasi-periodic feature of the flow in the QP state is induced by the unstable phase at which the head of the lower branch of the vortex tube is released into the wake, corresponding to the secondary instability by  $St_2$ . As  $St_2$  becomes dominant for slightly higher Reynolds numbers, this instability evolves into the streamwise fluctuations along with the regular vortex shedding, which undergoes approximately two cycles of oscillation over seven shedding periods.
- (vii) One of the unique characteristics in the HS2 state is that the Strouhal number  $St_1$  is commensurable with  $St_2$  with a ratio of  $St_1/St_2 = 7/2$ , suggesting a high-order synchronisation between the vortex shedding process and the flow features associated with the secondary instability. The physics behind the  $7/2$  synchronisation is that seven cycles of vortex shedding occur exactly over two secondary periods. By splitting the full period  $2T_2$  into two uneven intervals  $T_1$  and  $T_2$  in terms of the recurrence pattern on  $C_{l,z}$ , four hairpin-vortex shedding circles are established in  $T_1$  whilst three circles are found in  $T_2$ . The wake of the HS2 flow is featured by two relatively stable shedding periods due to the streamwise oscillation by the secondary instability. The flow mechanism behind this observation is that the relatively stable periods hinder the formation of merged vortex tubes of opposite signs.
- (viii) The onset of chaotic vortex shedding is marked by the breaking of the last flow symmetry about the  $y = 0$  plane for  $Re \geq 310$ . In the vicinity of the transition flow becomes unstable about the  $y = 0$  plane, where small amplitudes of random oscillations appear while the vortex shedding largely remains in the  $x-z$  plane.

The observations and understandings towards the secondary instability in the periodic shedding flows are pivotal to future studies on wake transition to turbulence for flow around a cube. It is anticipated that the low frequency will continue to play a significant role in the breaking of coherent structures into smaller-scale vortices at higher Reynolds numbers. When the breaking of symmetry occurs, the discontinuous symmetry of the cube will again start to strongly affect the development and evolution of the coherent structures in the wake.



Mesh	Cell number	$(N_x, N_{y,z})$	$\Delta x_w$	$\overline{C_d}$	$\overline{C_l}$	$C_l'$
1	3.14 million	(42, 30)	0.1325	0.8735	0.1105	0.03457
2	6.23 million	(61, 46)	0.1152	0.8728	0.1112	0.03417
3	9.76 million	(85, 61)	0.0996	0.8735	0.1101	0.03423

Table 3. Comparison of the time-averaged drag coefficient  $\overline{C_d}$ , lift coefficient magnitude  $\overline{C_l}$  and root-mean-square deviation of the lift coefficient magnitude  $C_l'$  obtained by the three meshes at  $Re = 400$ .

**Funding.** This research is funded by the Australian Government through Cooperative Research Centres Project (CRC-P) grant under project code CRC-P57367, which is in collaboration with Total Marine Technology Pty Ltd (<https://www.tmtrov.com.au>) as the industry lead of the project. The simulation work was conducted through the facility from Pawsey Supercomputing Centre with funding from the Australian Government and the Government of Western Australia.

**Declaration of interests.** The authors report no conflict of interest.

**Author ORCIDs.**

-  Qingrui Meng <https://orcid.org/0000-0002-1822-0971>;
-  Hongwei An <https://orcid.org/0000-0002-9082-1405>.

**Appendix A. Mesh dependence**

Mesh dependence is studied at the upper bound of  $Re$  range for the problem of interest, i.e.  $Re = 400$ . Three meshes are considered and the total number of cells is 3.14 million in mesh 1, doubled and tripled in meshes 2 and 3, respectively. The mesh refinement is only conducted in the internal region, whilst the total number of cells in the external region is maintained around 0.33 million for all meshes. Table 3 lists the details of the three meshes, where  $N_x$  and  $N_{y,z}$  are employed to denote the node numbers along the cube edges in  $x$ ,  $y$  and  $z$  directions, respectively;  $\Delta x_w$  represents the uniform streamwise dimension of the cells in the internal wake region  $x > 3.5$ .

The time-averaged hydrodynamic coefficients  $\overline{C_d}$  and  $\overline{C_l}$ , and the root-mean-square values of the lift coefficient magnitude  $C_l'$  are given in table 3. The maximum differences of  $\overline{C_d}$ ,  $\overline{C_l}$  and  $C_l'$  obtained by the three meshes are 0.08 %, 1 % and 1.17 %, respectively, suggesting these coefficients are insensitive to the resolutions of the three meshes.

The mesh dependence is further checked by comparing pressure distributions along selected middle lines on the cube surface and velocity distributions in the wake. For the pressure distribution, the pressure coefficient  $C_p$  is considered and defined as

$$C_p = \frac{p^*}{1/2\rho U^2}, \tag{A1}$$

where  $p^*$  is the dimensional form of the pressure.

Figures 27(a) and 27(b) show the time-averaged distributions of  $\overline{C_p}$  along two paths. The first path in figure 27(a) is represented by  $A \rightarrow B \rightarrow C \rightarrow D \rightarrow A$  with the midpoints situated at  $A (-0.5, 0.5, 0)$ ,  $B (0.5, 0.5, 0)$ ,  $C (0.5, -0.5, 0)$  and  $D (-0.5, -0.5, 0)$ ; the second one in figure 27(b) is by  $A' \rightarrow B' \rightarrow C' \rightarrow D' \rightarrow A'$  with  $A' (-0.5, 0, 0.5)$ ,  $B' (0.5, 0, 0.5)$ ,  $C' (0.5, 0, -0.5)$  and  $D' (-0.5, 0, -0.5)$ . It is noted that the time-averaged pressure coefficients are in good agreement with each other along every path, indicating the distributive forces on the cube are converged for the three meshes. In figures 27(a) and 27(b), the value of  $\overline{C_p}$  at the stagnation point of the front face of the cube is shown

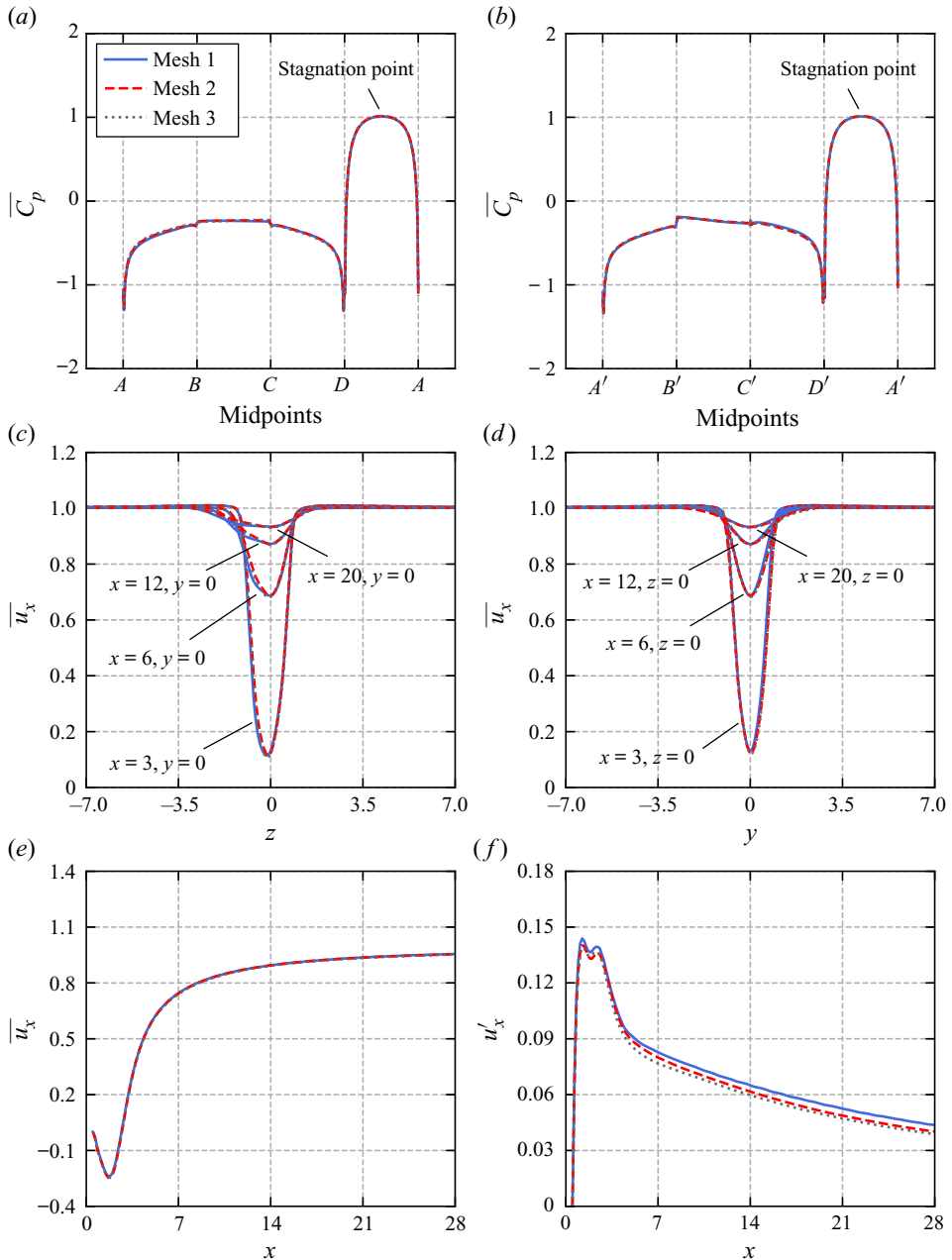


Figure 27. Convergence study for the distribution of the pressure coefficient  $C_p$  along paths on the cube, and streamwise velocity  $u_x$  along lines in the wake, where the overline and prime notations denote the mean value and root-mean-square deviation, respectively. Plots of (a)  $\overline{C_p}$  along  $A \rightarrow B \rightarrow C \rightarrow D \rightarrow A$  and (b)  $\overline{C_p}$  along  $A' \rightarrow B' \rightarrow C' \rightarrow D' \rightarrow A'$ , where  $A, B, C$  and  $D$  are the midpoints of the cube edges on the plane  $z = 0$ , while  $A', B', C'$  and  $D'$  are those on plane  $y = 0$ . For coordinates of the midpoints, see the discussion. Plots of (c)  $\overline{u_x}$  on the lines intersected by planes  $x = 3, 6, 12, 20$  and  $y = 0$ , and (d)  $\overline{u_x}$  on the lines by planes  $x = 3, 6, 12, 20$  and  $z = 0$ . Plots (e, f) are  $\overline{u_x}$  and  $u'_x$  along the streamwise central line in the wake.

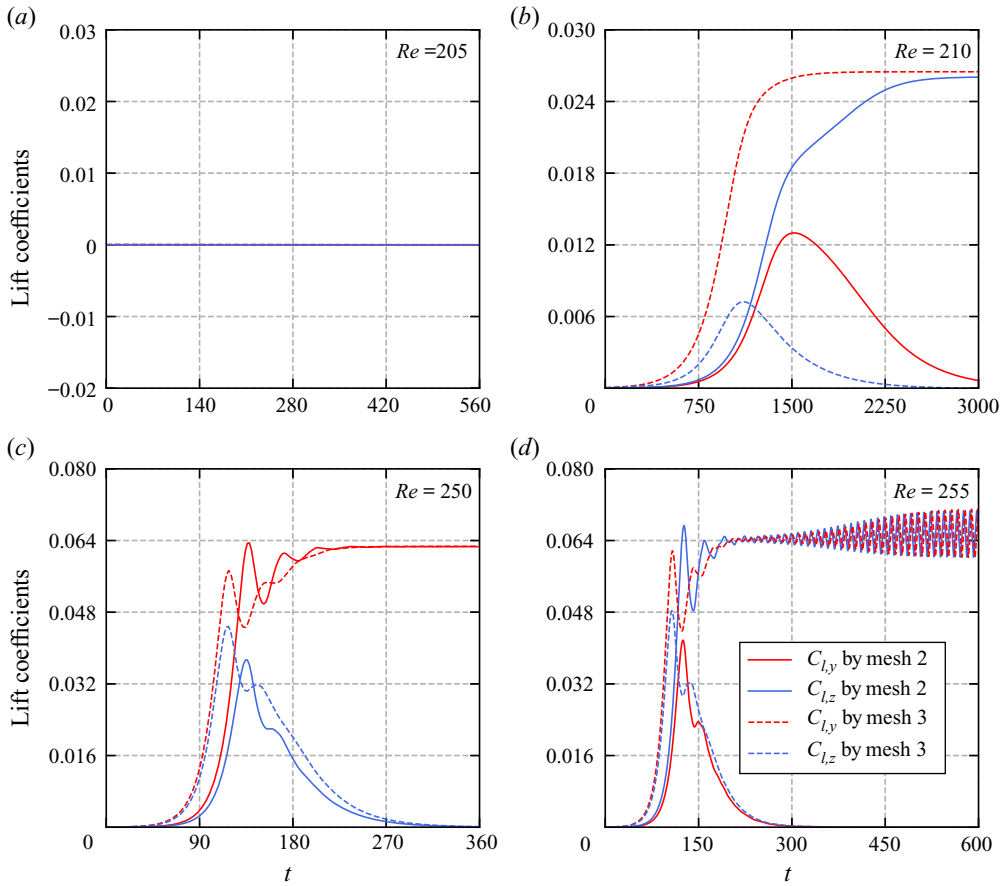


Figure 28. Mesh dependence study for the transitional ranges of the regular and Hopf bifurcations, where the time histories of the lift coefficients  $C_{l,y}$  and  $C_{l,z}$  for the cases (a)  $Re = 205$ , (b)  $Re = 210$ , (c)  $Re = 250$  and (d)  $Re = 255$  are obtained based on meshes 2 and 3 in table 3.

approximately equal to 1, which demonstrates that the distance between the cube and the inlet is appropriate.

The time-averaged velocity component  $\overline{u_x}$  in the specific locations of the wake are plotted in figures 27(c), 27(d) and 27(e). Figure 27(c) shows the results along the lines intersected by the planes  $x = 3, 6, 12, 20$  with  $y = 0$ , figure 27(d) is along the lines by  $x = 3, 6, 12, 20$  with  $z = 0$  and figure 27(e) is along the central line by  $y = 0$  and  $z = 0$ . It is noted that the profiles of the mean streamwise velocity based on the three meshes agree very well with each other. The root-mean-square value of streamwise velocity  $u'_x$  along the central line is plotted in figure 27(f). The profiles of  $u'_x$  based on mesh 2 and mesh 3 agree reasonably well, while the one based on mesh 1 deviates noticeably from other two shown in figure 27(f). The following quantitative measure  $\chi_{mn}$  is employed to compare the difference of  $u'_x$  values obtained based on mesh  $m$  and  $n$ ,

$$\chi_{mn} = \frac{\int |u'_{x,m} - u'_{x,n}| dx}{\int |u'_{x,n}| dx}. \quad (\text{A2})$$

Here  $\chi_{13} \approx 7.9\%$  and  $\chi_{23} \approx 2.9\%$  are obtained, which is consistent with the qualitative observation discussed above.

The results presented above show that mesh refinement based on mesh 2 improves little on the accuracy. Mesh 2 is thereby selected for all the simulations.

We have examined the critical values of Reynolds number for the regular transition at  $Re_{cr}^{RT} \approx 207.0$  and for the Hopf transition at  $Re_{cr}^{HT} \approx 252.0$ . To verify the convergence of these critical Reynolds numbers regarding the mesh density, mesh 3 is further employed to simulate the cases at the upper and lower bounds of the  $Re$  ranges for the regular and Hopf bifurcations, i.e.  $Re = 205, 210, 250$  and  $255$ , in comparison with the results by mesh 2. The time histories of  $C_{l,y}$  and  $C_{l,z}$  are plotted in figure 28 to verify the spatial symmetry and temporal development. It is noted that the total cell number increases by 56.7 % from mesh 2 to 3, and the transitional ranges of  $Re$  for the regular and Hopf bifurcations identified by the two meshes are consistent. The differences of the mean values of  $C_d$ ,  $C_l$  and  $St_1$  in the four cases are all in the magnitude of order  $10^{-4}$ – $10^{-5}$ . Therefore, the transitional  $Re$  ranges in our simulation results are independent of the meshes. Mesh 1 is further employed to check the QP and HS2 flows, and the same transition route is observed in  $280 \leq Re \leq 300$ , which means the occurrence of the secondary frequency is also independent of the meshes.

## REFERENCES

- ARMSTRONG, M.A. 2013 *Groups and Symmetry*. Springer Science & Business Media.
- BOHORQUEZ, P., SANMIGUEL-ROJAS, E., SEVILLA, A., JIMÉNEZ-GONZÁLEZ, J.I. & MARTINEZ-BAZAN, C. 2011 Stability and dynamics of the laminar wake past a slender blunt-based axisymmetric body. *J. Fluid Mech.* **676**, 110–144.
- CHENG, L., JU, X., TONG, F. & AN, H. 2020 Transition to chaos through period doublings of a forced oscillating cylinder in steady current. *J. Fluid Mech.* **887**, A5.
- GAO, S., TAO, L., TIAN, X. & YANG, J. 2018 Flow around an inclined circular disk. *J. Fluid Mech.* **851**, 687–714.
- GRIFFIN, O.M. 1995 A note on bluff body vortex formation. *J. Fluid Mech.* **284**, 217–224.
- HAIDER, A. & LEVENSPIEL, O. 1989 Drag coefficient and terminal velocity of spherical and nonspherical particles. *Powder Technol.* **58** (1), 63–70.
- ISSA, R.I. 1986 Solution of the implicitly discretised fluid flow equations by operator-splitting. *J. Comput. Phys.* **62** (1), 40–65.
- JEONG, J. & HUSSAIN, F. 1995 On the identification of a vortex. *J. Fluid Mech.* **285**, 69–94.
- JIANG, H. & CHENG, L. 2020 Flow separation around a square cylinder at low to moderate Reynolds numbers. *Phys. Fluids* **32** (4), 044103.
- JU, X., AN, H., CHENG, L. & TONG, F. 2020 Modes of synchronisation around a near-wall oscillating cylinder in streamwise directions. *J. Fluid Mech.* **893**, A8.
- KHAN, M.H., SHARMA, A. & AGRAWAL, A. 2020 Simulation of flow around a cube at moderate Reynolds numbers using the lattice Boltzmann method. *Trans. ASME J. Fluids Engng* **142** (1), 011301.
- KLOTZ, L., GOUJON-DURAND, S., ROKICKI, J. & WESFREID, J.E. 2014 Experimental investigation of flow behind a cube for moderate Reynolds numbers. *J. Fluid Mech.* **750**, 73–98.
- LEE, S. 2000 A numerical study of the unsteady wake behind a sphere in a uniform flow at moderate Reynolds numbers. *Comput. Fluids* **29** (6), 639–667.
- PIKOVSKY, A., ROSENBLUM, M. & KURTHS, J. 2003 *Synchronization: A Universal Concept in Nonlinear Sciences*. Cambridge Nonlinear Science Series, vol. 12. Cambridge University Press.
- REN, C., CHENG, L., TONG, F., XIONG, C. & CHEN, T. 2019 Oscillatory flow regimes around four cylinders in a diamond arrangement. *J. Fluid Mech.* **877**, 955–1006.
- RICHTER, A. & NIKRITYUK, P.A. 2012 Drag forces and heat transfer coefficients for spherical, cuboidal and ellipsoidal particles in cross flow at sub-critical Reynolds numbers. *Intl J. Heat Mass Transfer* **55** (4), 1343–1354.
- SAHA, A.K. 2004 Three-dimensional numerical simulations of the transition of flow past a cube. *Phys. Fluids* **16** (5), 1630–1646.
- SAU, A. 2009 Hopf bifurcations in the wake of a square cylinder. *Phys. Fluids* **21** (3), 034105.
- SEYED-AHMADI, A. & WACHS, A. 2019 Dynamics and wakes of freely settling and rising cubes. *Phys. Rev. Fluids* **4** (7), 074304.

*Wake transitions behind a cube in Re 1–400*

- SHEARD, G.J., THOMPSON, M.C. & HOURIGAN, K. 2004 From spheres to circular cylinders: non-axisymmetric transitions in the flow past rings. *J. Fluid Mech.* **506**, 45–78.
- STUART, J.T. 1960 On the non-linear mechanics of wave disturbances in stable and unstable parallel flows. Part 1. The basic behaviour in plane Poiseuille flow. *J. Fluid Mech.* **9** (3), 353–370.
- THOMPSON, M.C., HOURIGAN, K., RYAN, K. & SHEARD, G.J. 2006 Wake transition of two-dimensional cylinders and axisymmetric bluff bodies. *J. Fluids Struct.* **22** (6–7), 793–806.
- THOMPSON, M.C., LEWEKE, T. & PROVANSAL, M. 2001 Kinematics and dynamics of sphere wake transition. *J. Fluids Struct.* **15** (3–4), 575–585.
- TOMBOULIDES, A.G. & ORSZAG, S.A. 2000 Numerical investigation of transitional and weak turbulent flow past a sphere. *J. Fluid Mech.* **416**, 45–73.
- TRAN-CONG, S., GAY, M. & MICHAELIDES, E.E. 2004 Drag coefficients of irregularly shaped particles. *Powder Technol.* **139** (1), 21–32.
- WATSON, J. 1960 On the non-linear mechanics of wave disturbances in stable and unstable parallel flows. Part 2. The development of a solution for plane Poiseuille flow and for plane Couette flow. *J. Fluid Mech.* **9** (3), 371–389.